

TWINNED BOUNDARIES IN NANOMATERIALS

R.A. Andrievski

Institute of Problems of Chemical Physics, Russian Academy of Sciences, Semenov Prospect 1,
Chernogolovka, Moscow Region, 142432, Russia

Received: March 10, 2016

Abstract. This overview outlines the current state of the nanotwinned structures studies in metallic nanomaterials. The various processes of twin generation, such as the pulse electrodeposition technique, magnetron sputtering and different variants of severe plastic deformation (equal channel angular pressing, high pressure torsion, accumulative roll bonding, and surface mechanical grinding/rolling treatment, etc.), are described. The structural characterization of the growth/deformation twins by transmission electron microscopy methods, including high-resolution one, is discussed. Special attention is given to a surface mechanical grinding/rolling treatment for the gradient structure formation with a high content of low-angle twinned boundaries. The influence of nanotwinned structure on the nanomaterials strength, ductility, fatigue properties, electrical conductivity, especially under extreme conditions (such as high temperatures, irradiation and corrosion actions) is discussed in details. A significant increase of these properties as compared with conventional nanomaterials is underlined. In many cases, the nanomaterials with the nanotwinned and gradient structure remain tolerant to the various extreme conditions, such as high temperature heating, irradiation, deformation and corrosion actions. Some poorly researched aspects are also put into considerations.

1. INTRODUCTION

It is well known that the twin formation is connected and accompanied with the plastic deformations and can manifest itself in the growth of crystals, for example, in the processes of electrodeposition and physical vapor deposition coatings (so-called deformation and growth twins). Interest in the nanotwinned structures in metal base nanomaterials has increased significantly in connection with results of Lu, Zhang, and co-authors [1-3]. The most interesting information of these investigations was obtained using Cu samples with nanotwinned structure and can be formulated as follows:

- it was discovered that these samples had the high values of strength and electrical conductivity, considering that nanotwinned boundaries present an effective blockage for the dislocation motion, but at the same time remain permeable for conduction electrons [1];

- it has been shown that from the high strength combination with a good ductility there follows a known Hall–Petch relation by taking the twin lamellar thickness (λ), being equivalent grain size (d) [2];
- it was noted that sputtered films have remarkable thermal stability after annealing at 800 °C ($0.74 T_m$, where T_m is the melting point of Cu) much on this indicator superior to conventional copper nanomaterials [3].

These results seem to be interesting for the development of such areas as the identification of nanomaterials with the high level of physical/mechanical stable properties and the establishment of appropriate theoretical approaches. In our previous studies [4], some problems of the nanomaterials tolerance under extremes were analyzed, but the need of more detailed considerations and continuous updating of the data seem to be compelling reasons to return to these issues.

Corresponding author: R.A. Andrievski, e-mail: ara@icp.ac.ru

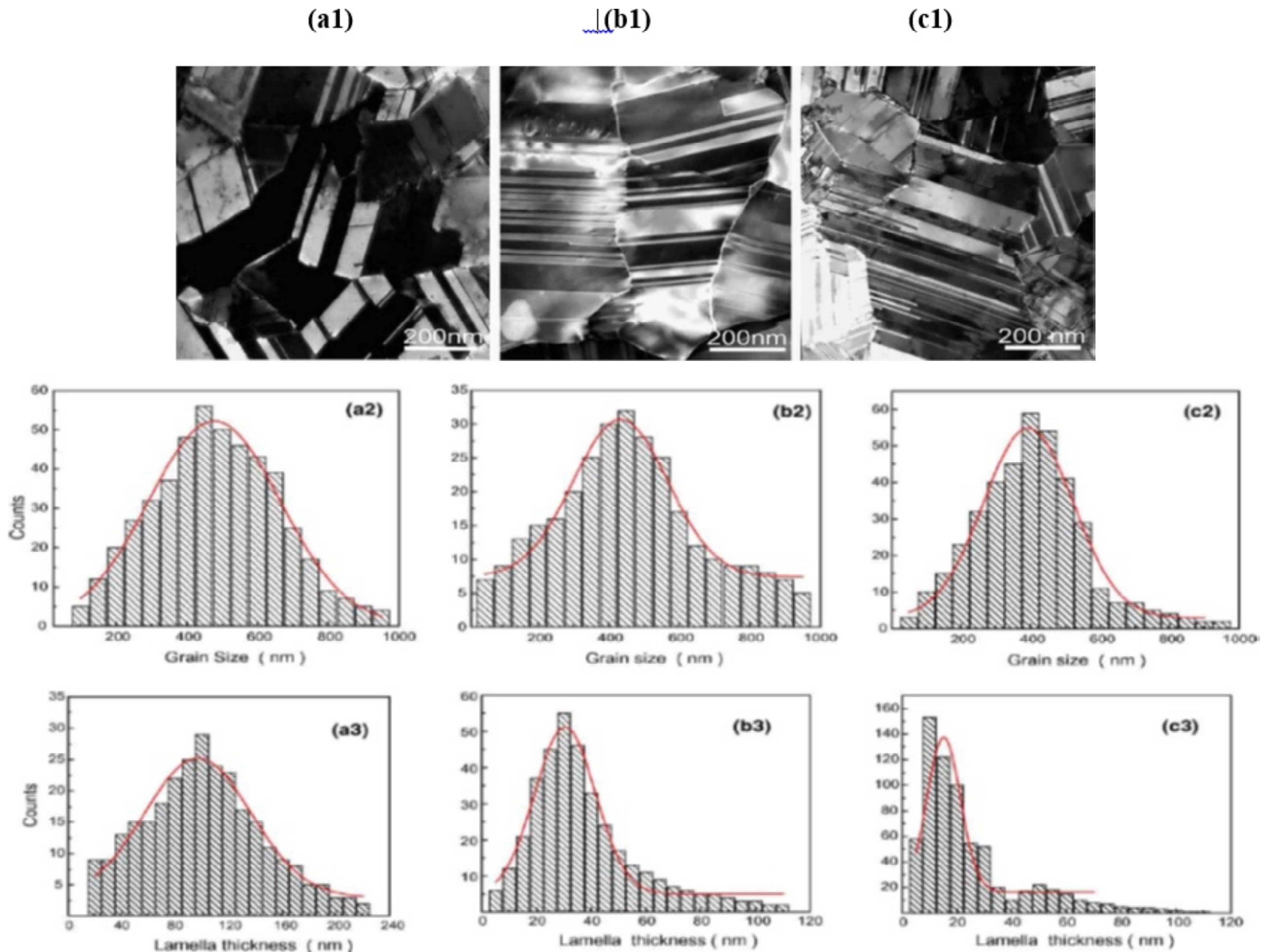


Fig. 1. TEM images (a1, b1, and c1), histograms of grain size distributions (a2, b2, and c2) and twin lamellar thickness distributions (a3, b3, and c3) in three as-deposited Cu samples (A, B, and C), respectively (adapted from [2]).

2. GENERAL INFORMATION ON TWINNED STRUCTURES AND METHODS OF THEIR PRODUCING

2.1. Growth twins

Fig. 1 shows typical bright field transmission electron microscopy (TEM) images for three as-deposited copper samples (a1, b1, and c1) with the same average grain size ($d = 400\text{--}450$ nm), but with different average twin lamellar thickness ($15\text{ nm} < \lambda < 100$ nm). There are also shown the histograms of the grain size and lamella thickness distributions (a2, b2, c2, a3, b3, and c3), respectively. The range of lamellas density is from 0.8 to $5.3 \times 10^7\text{ m}^{-1}$. According to X-ray diffraction (XRD) analysis, all electrodeposited objects have texture (110). As you can see from TEM images (a1, b1, and c1), lattice dislocations inside the lamellas are not observed. The use of high-resolution TEM (HRTEM) has allowed the establish the fact that most twinned boundaries are coherent with the lattice with coincidence of $\Sigma 3$

interface, associated with the Shockley partial dislocations presence, as indicated in the insert of Fig. 2b.

From general thermodynamic considerations, the formation of twins leads to a total interface energy decrease, because the excess energy for coherent twinned boundaries is much smaller than this energy in the case of the samples with conventional high-angle grain boundaries. Some high purity copper samples (99.995%) in the form of a foil (thickness and length of $30\text{ }\mu\text{m}$ and $10\text{--}20$ mm, respectively) with nanotwinned structure (Figs. 1 and 2) were obtained by pulsed electrodeposition from a solution of CuSO_4 [1,2,5], and in contrast to conventional modes of direct current, these pulsed electrodeposition allows the use of high current density with a short period time of 0.02 s to achieve a very high deposition rate (up to 10 nm/s) contributing to the nucleation sites increase and their growth.

Let us consider other examples of growth twins. Fig. 3 shows the cross-sections of sputter-depos-

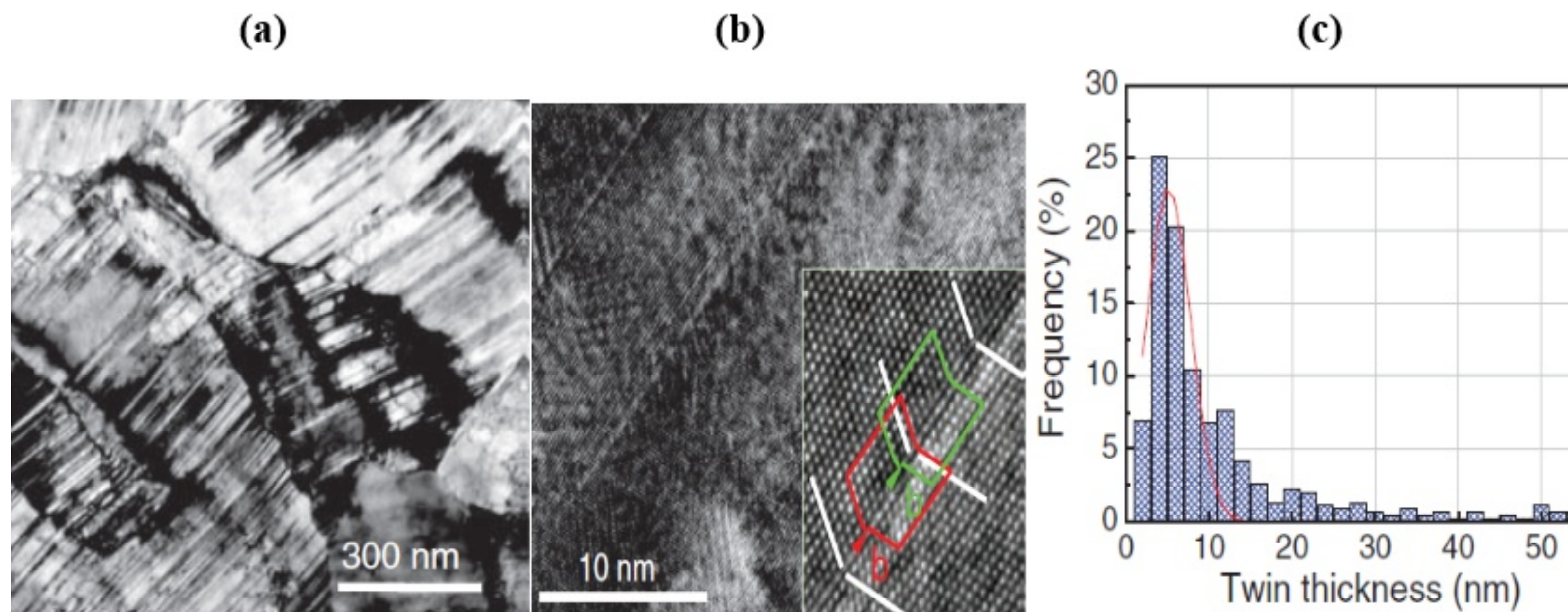


Fig. 2. TEM and HRTEM images of as-deposited Cu sample with the finest twins (**a** and **b**, respectively) and the distribution of the twin lamellar thickness (**c**) (adapted from [5]).

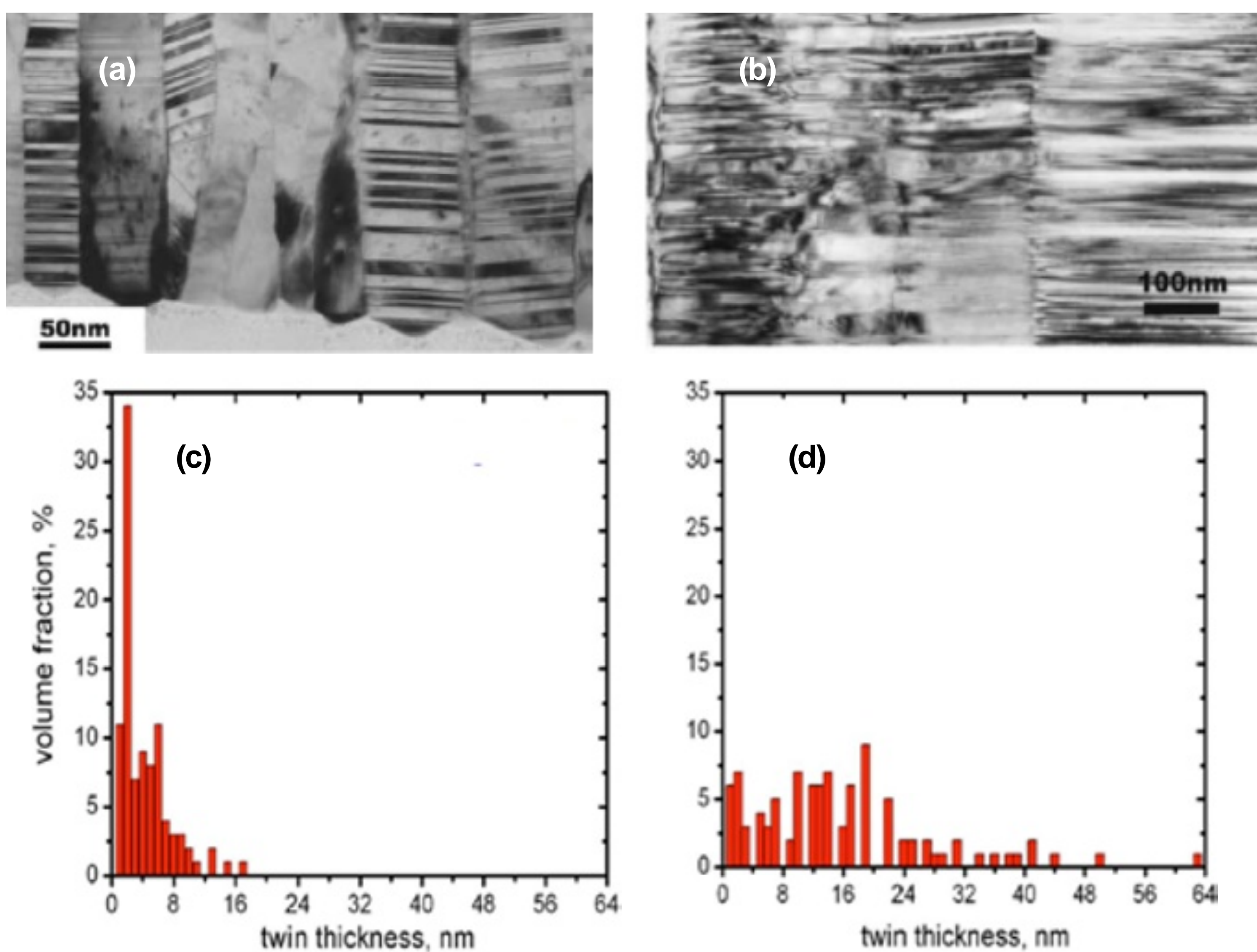


Fig. 3. Cross-section TEM images of Cu films in as-deposited state (**a**) and after annealing at 800 °C (**b**) as well as corresponding statistical distributions of twin lamellar thickness of as-deposited (**c**) and annealed (**d**) samples (adapted from [3]).

ited Cu films in the as-deposited state and after annealing at 800 °C; the histograms of the twin thickness are also shown in Fig. 3.

As is evident from Figs. 3a and 3c, the as-deposited films with a thickness of 33 μm have a columnar structure with a (111) texture along the direction of growth (an average grain size $d \sim 43$ nm) and are characterized by a high density of twins, oriented parallel to surface deposition, with the mean value λ of about 4 nm. Some fixed planar defects

were identified to be stacking faults. HRTEM has allowed establish the fact that the boundaries between the lamella surfaces and columnar interfaces have low-angle grain boundary, approximately 9°.

As it can also be seen from Figs. 3b and 3d, an annealing at 800 °C leads to a broader distribution in the twin thickness with the average value of λ changing up to ~ 16 nm, but the general columnar structure remains valid. Films, demonstrated in Figs. 3a and 3b, were fabricated by magnetron sputtering

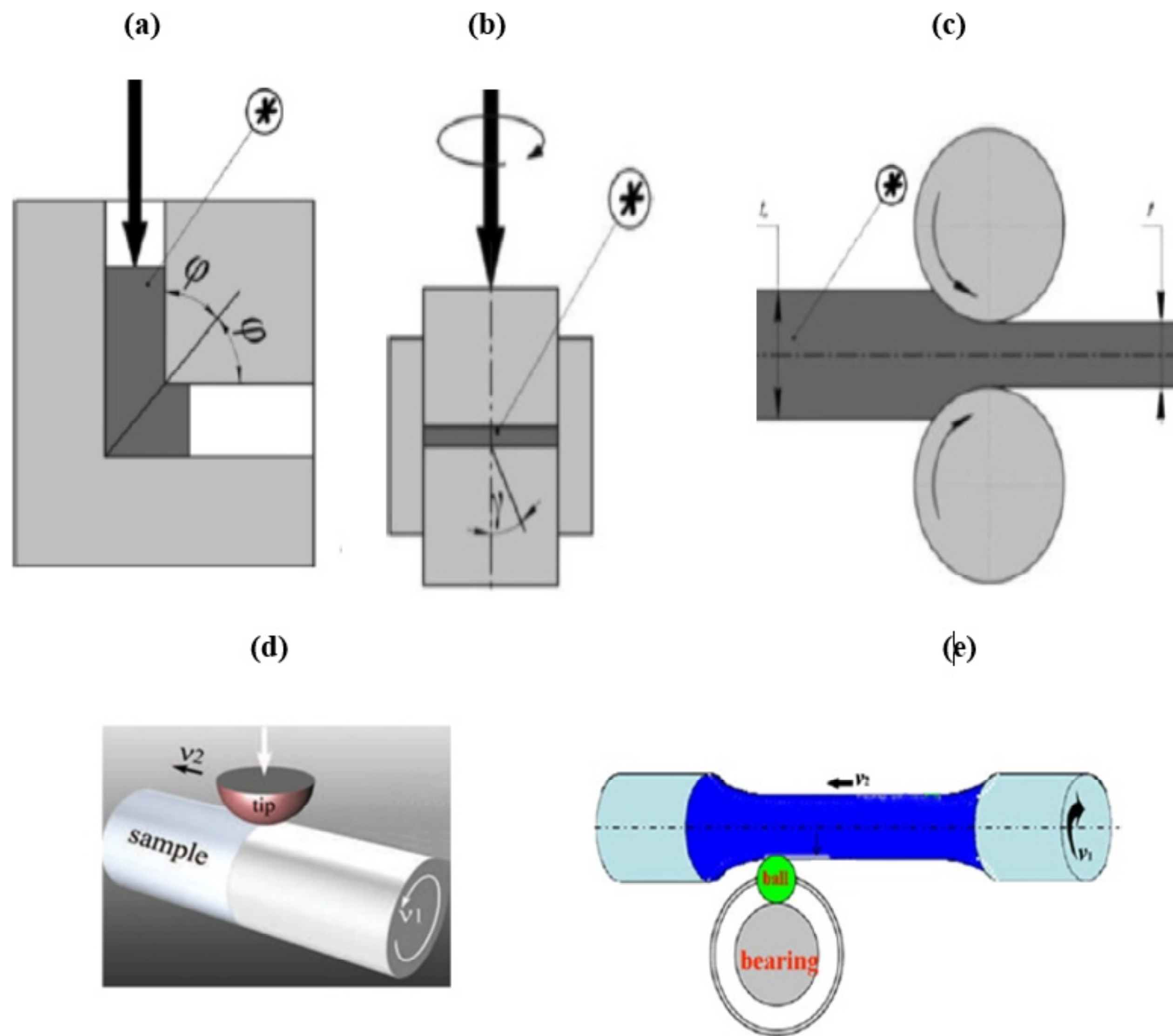


Fig. 4. Schematic illustration of some SPD techniques: (a) ECAP; (b) HPT; (c) ARB (a conventional sign* is a designation for initial sample; adapted from [7]); (d) SMGT (adapted from [8]); (e) SRT (adapted from [9]).

of Cu (99.999%) target at the deposition rate of 2 nm/s on Si (100) substrate with a native SiO_2 layer [3]. Annealing of freestanding films was carried out in vacuum $\leq 5 \times 10^{-7}$ torr for 1 hour.

The study of interfaces in Ag/Ni, Ag/Al, Cu/Fe, and Cu/Ni multilayer films prepared by magnetron sputtering allowed receive the basic criteria for formation of growth twins in high stacking fault energy face-centered cubic (FCC) metals [6]. These two criteria can be formulated by following: (1) a low stacking fault energy buffer layer that facilitates the occurrence of twin seeds and (2) global coherence between the coherent similar interfaces or local coherence between coherent dissimilar interfaces that permits twins to propagate across layer interfaces.

2.2. Deformation twins

Fig. 4 shows the basic schemes of severe plastic deformation (SPD) used for deformation effects in nanomaterials: equal channel angular pressing (ECAP), high pressure torsion (HPT), accumulative roll bonding (ARB), surface mechanical grinding/attrition treatment (SMGT/SMAT), and surface rolling treatment (SRT). Traditional technological schemes

of ECAP and HPT are aimed at creating a more or less uniform nano- and ultrafine-grained (UFG) materials and lead to a significant increase in strength due to of lattice dislocations number increase and the high-angle boundaries formation [7].

General regularities of the deformation twins formation in nanomaterials, including experimental data and results of simulation by molecular dynamics (MD), are discussed by Zhu, Liao, and Wu in detail [10]. It is emphasized that the metals with FCC structure are the most studied and objects with hexagonal close-packed (HCP) and body-centered cubic structure need in further investigation. In addition, it is important to note that the twins formation in FCC nanometals, flowing much faster compared to their coarse-grained counterparts, reveals a dependence on energy of stacking faults (γ , mJ m^{-2}). Thus in the case of Ag ($\gamma \sim 15$), Cu ($\gamma \sim 40$), and Ni ($\gamma \sim 120$), a higher density of twins (particularly having the smallest thickness of twin lamella) is observed for silver. It is also interesting to note that in polycrystalline Ni ($d \sim 40 \mu\text{m}$) after SMAT, deformation twins were only observed when the grain size is $d < 100 \text{ nm}$, while the larger grain sizes were fixed dislocation plasticity [11]. The propensity for twinning increases with decreasing grain size

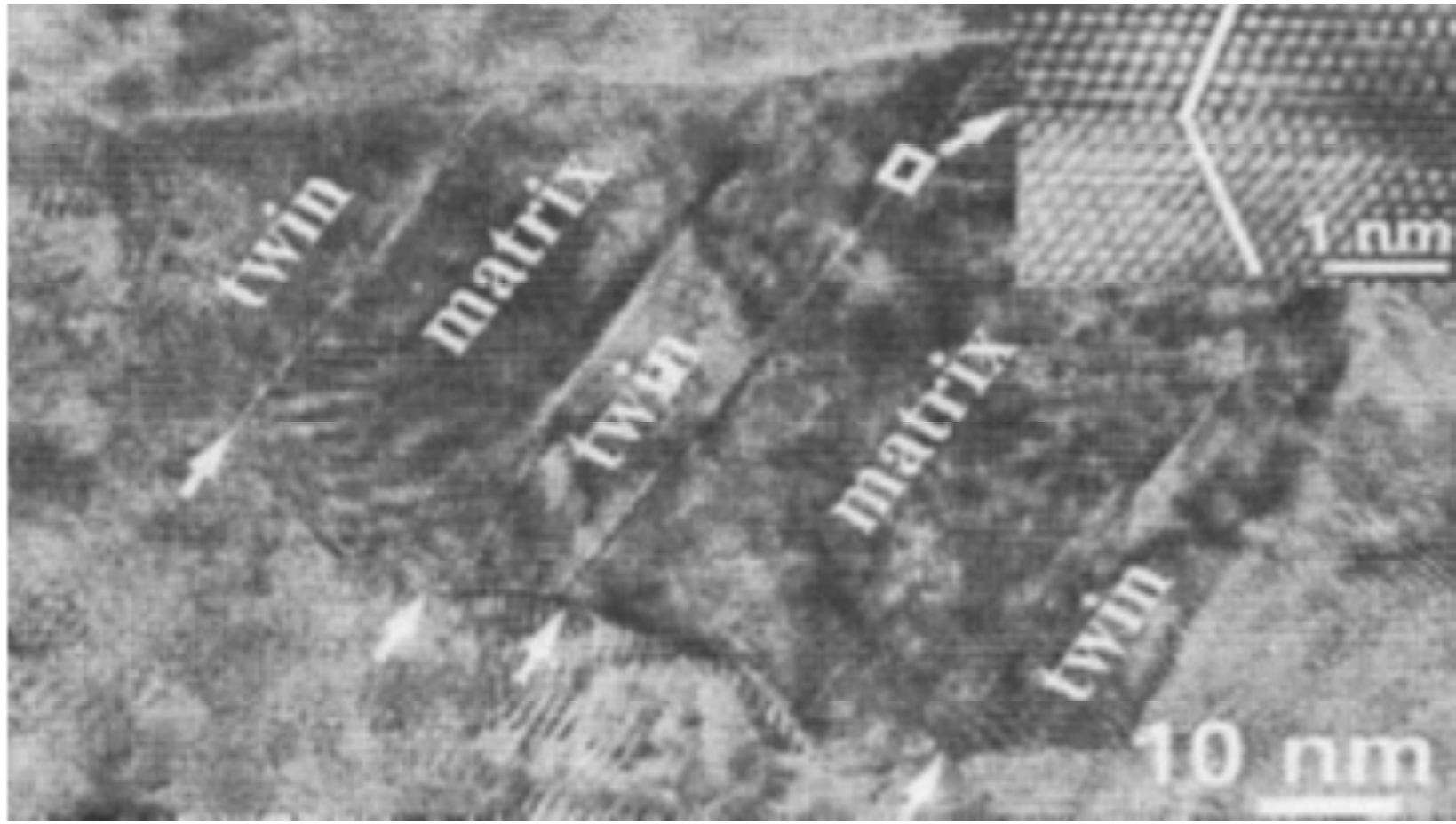


Fig. 5. TEM image of deformation twins in the nanostructured Ni grain. Arrows indicate the twin boundaries; the inset shows a HRTEM image of the framed area enclosing a twin boundary (adapted from [11]).

and deformation temperature as well with a strain rate increasing. The inverse grain size effect on twinning is observed in Ni samples with a grain size less than 50 nm [12].

Fig. 5 shows deformation twinning occurring in a Ni grain of ~ 80 nm. It is assumed that the twin formation is occurred due to the heterogeneous emission of Shockley partial dislocations with Burgers vector of type $a/6$ [11 $\bar{2}$].

Comparison of various SPD methods in relation to the nanotwinned structures formation in a model alloy Cu–30 wt.%Zn with low energy of stacking faults ($\gamma \sim 7$ mJ m $^{-2}$, that is, with a high degree of the deformation twins formation) was conducted in Ref. [13]. The original samples (diameter of 10 mm and thickness of 0.8 mm), were subjected to of ECAP and HPT treatments as well as additional rolling after ECAP with a thickness reduction of 75% and 95%. The main results of the determination of grain size, thickness and density of twins, as well as matrix spaces are given in Table 1.

It is evident from Table 1 that the ECAP and HPT processing leads to low values of ρ_t and the highest density of twins, as is observed after ECAP+ 95% rolling, that does not depend monotonically on the

values of grain size and thickness of twins and matrix spaces.

Here, we will shortly describe the possibilities SMGT and SRT methods [8,9], deliberately designed to form the gradient structures with a high content of low-angle twinned boundaries. Fig. 6 shows typical bright-field cross-sectional and longitude-sectional TEM images of the structure at different distances from the sample surface Ni processed by SMGT; the corresponding histograms of the distribution of grain sizes are also shown (adapted from [8]). It is clearly visible from Fig. 6 that the grain structure change depends on the distance from the surface of the processing (h). The structure study by various methods, including electron back-scattering diffraction (EBSD), has showed that the nanostructured layer ($d < 100$ nm) extends to a depth of about 80 μ m. At the very top-layer ($h < 10$ μ m), the value of d is about 11 nm, and at $h = 10$ –50 μ m, the average value of d was equal to 18 ± 5 nm. The grains disorientation varied in a small angular range from 1° to 8° . The low-angle boundaries part at the depth $h = 40$ μ m in the transverse grain size $d = 20$ nm is about 100%. UFG structure was observed in the layer of 80–140 μ m and the presence of defects (dislocations and subgrains) was detected up to 1 mm depth (that corresponds to about 20% of the deformed zone magnitude for the original radius size). The share of low-angle boundaries at the depth of $h = 120$ μ m in the transverse grain size ($d = 180$ nm) is about 20% also.

A detailed study of gradient structures in HCP Ti produced by SRT was performed using XRD, TEM, EBSD, and scanning electron microscopy (SEM) [9]. Fig. 7 demonstrates the effect of distance from the surface for the processed sample (initial radius of 8 mm) on the size of grains (subgrains).

As can be seen from Fig. 7, the nanostructured layer with grain/subgrain size $d < 100$ nm is observed to a depth $h < 70$ μ m. In region I, deformation is carried out predominantly due to a formation of deformation twins with texture type

Table 1. The values of average grain size (d), twin lamellar thickness (λ_t), matrix width (λ_m), and twin density (ρ_t) of the ECAP, ECAP + 75% rolling, ECAP + 95% rolling, and HPT Cu–30 wt.%Zn samples (adapted from [13]).

| Treatment | d (nm) | λ_t (nm) | λ_m (nm) | ρ_t (10^6 m $^{-1}$) |
|------------------|----------|------------------|------------------|-------------------------------|
| ECAP | 3000 | 90 | 177 | 3.5 |
| ECAP+75% rolling | 355 | 17 | 32 | 6.9 |
| ECAP+95% rolling | 110 | 12 | 24 | 11.2 |
| HPT | 70 | 11 | 31 | 8.3 |

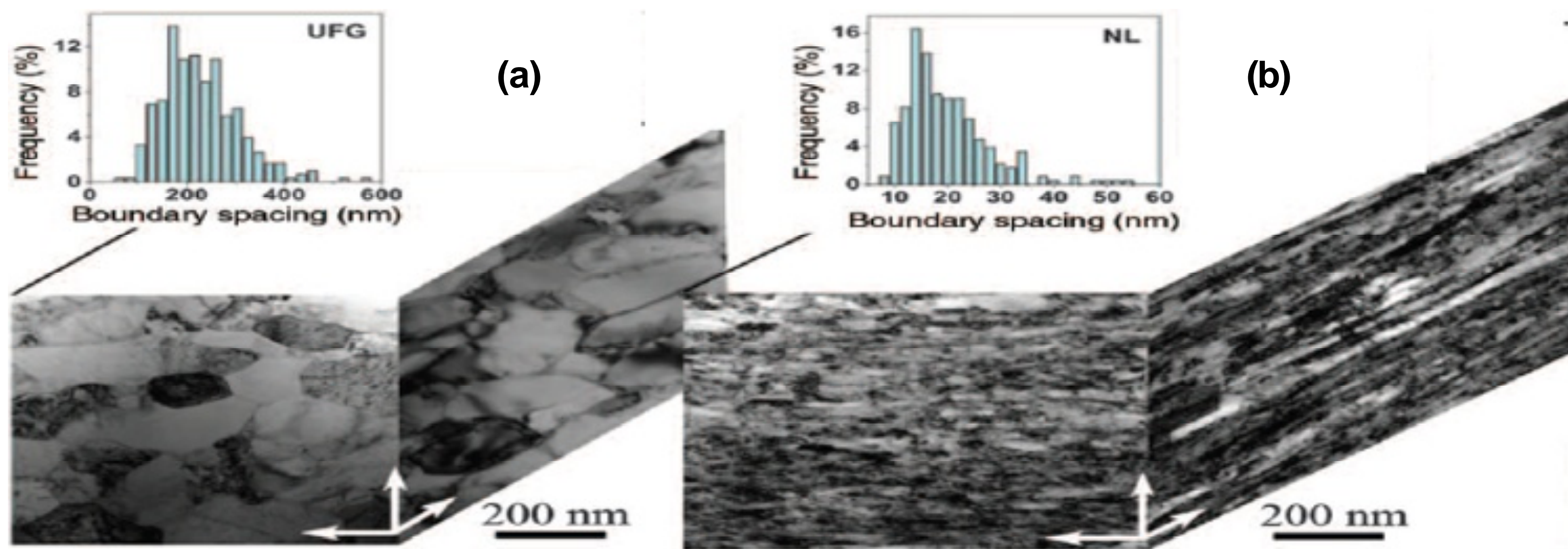


Fig. 6. Cross-sectional (a) and longitudinal-sectional (b) TEM images of ultrafine-grained (UFG; 110 μm deep from the surface) structure and nanometer-thick laminated (NL; 40–50 μm deep from the surface) structure of the Ni sample processed by SMGT. Inserts in (a) and (b) are the corresponding distribution of boundary spacing (adapted from [8]).

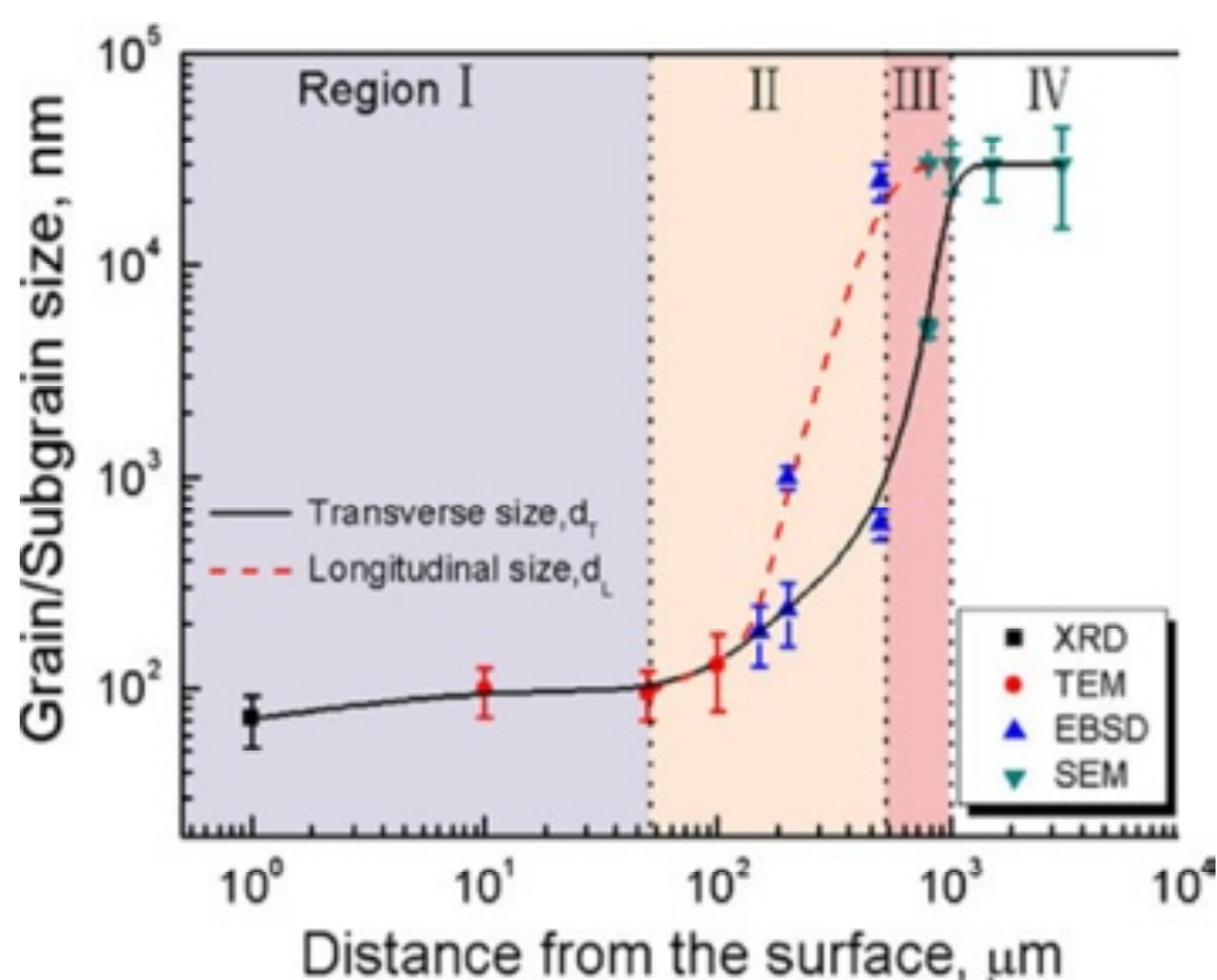


Fig. 7. The grain/subgrain size (under XRD, TEM, EBSD, and SEM data) vs. distance from surface of Ti sample processed by SRT. The region (I–IV) designations see in text (adapted from [9]).

$\{10\bar{1}2\}\langle 10\bar{1}1\rangle$. With distance h increasing (regions II and III) and enhancement of grain/subgrain size d , deformation attains more and more dislocation character with transformation of low-angle boundaries to the high-angle ones. At a distance $h > 800 \mu\text{m}$ (region IV), the original grain size is observed.

A comparison of deformation effects in FCC Cu and HCP Ti, processed by SMGT and SRT [8,9], shows that these results have much in common: a gradient distribution of grain size, a primary formation of nanotwins with low-angle boundaries in surface layers, the relatively small extent of surface nanostructured layers (70–80 μm) and total deformation zones (approximately 10–20% of the initial radius). Being similar in texture and size the resulting new twins are naturally different: Cu $\{100\}\langle 001\rangle$ and Ti $\{10\bar{1}2\}\langle 10\bar{1}1\rangle$ as textures typical for FCC and HCP metals.

The possibility of such SPD method as ARB (Fig. 4c) to create nanotwinned layers in two-phase systems consisting of immiscible (or partially soluble in each other) components should also be noted. This is especially evident in the example of Cu/Nb multilayer nanocomposites, electron microscopic images of which are shown in Fig. 8.

At ARB processing, the original many layered Cu/Nb billet is subjected to high degrees of deformation, during which the initial individual thickness is reduced from 2 mm to 10–20 nm. As can be seen from Fig. 8, the Cu/Nb nanocomposite in the final form has a layered structure, and nanoscale facets form with a zigzag-like morphology.

3. PROPERTIES OF NANOTWINNED STRUCTURES

3.1. Mechanical and electrical characteristics

Mechanisms of the twins influence on the nanomaterials strength and ductility are discussed in many papers (see references in the review [10], among which results [15–17] are the significant and interesting). The schemes of different strengthening mechanisms (with solute atoms, dispersed particles, the dislocation forest, and grain/twin boundaries) are presented in Fig. 9.

While traditional methods of the material strength increasing (Figs. 9a and 9b) are accompanied with a plasticity decrease, the increase due to nanotwins number is beneficial for both strength and ductility. In this case (Fig. 9c), it is assumed [1] that the interaction between full dislocations and twins leads to the formation of Shockley partially dislocations (with the Burger vector $b=1/6[1\bar{2}1]$), easily moving

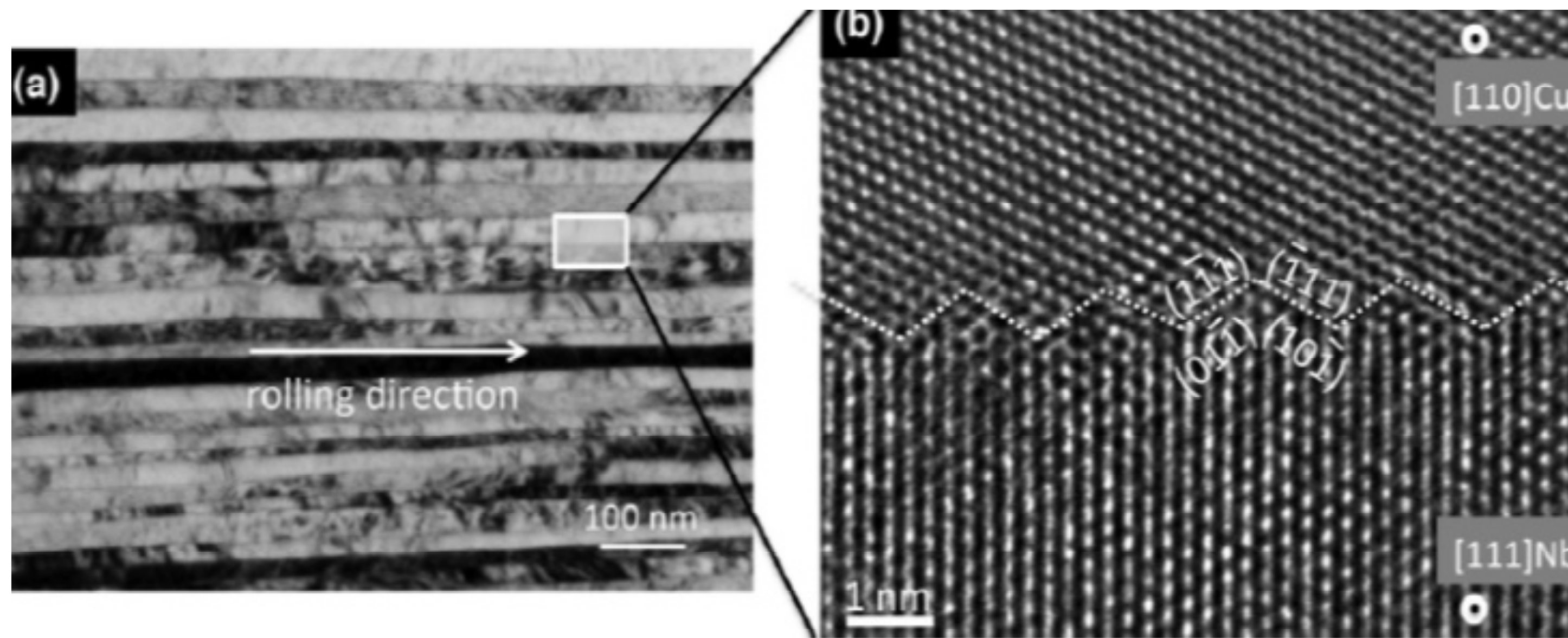


Fig. 8. TEM (a; monolayer thickness is of 20 nm) and HRTEM (b; monolayer thickness is of 10 nm) images of the Cu/Nb nanocomposite produced by ARB (adapted from [14]).

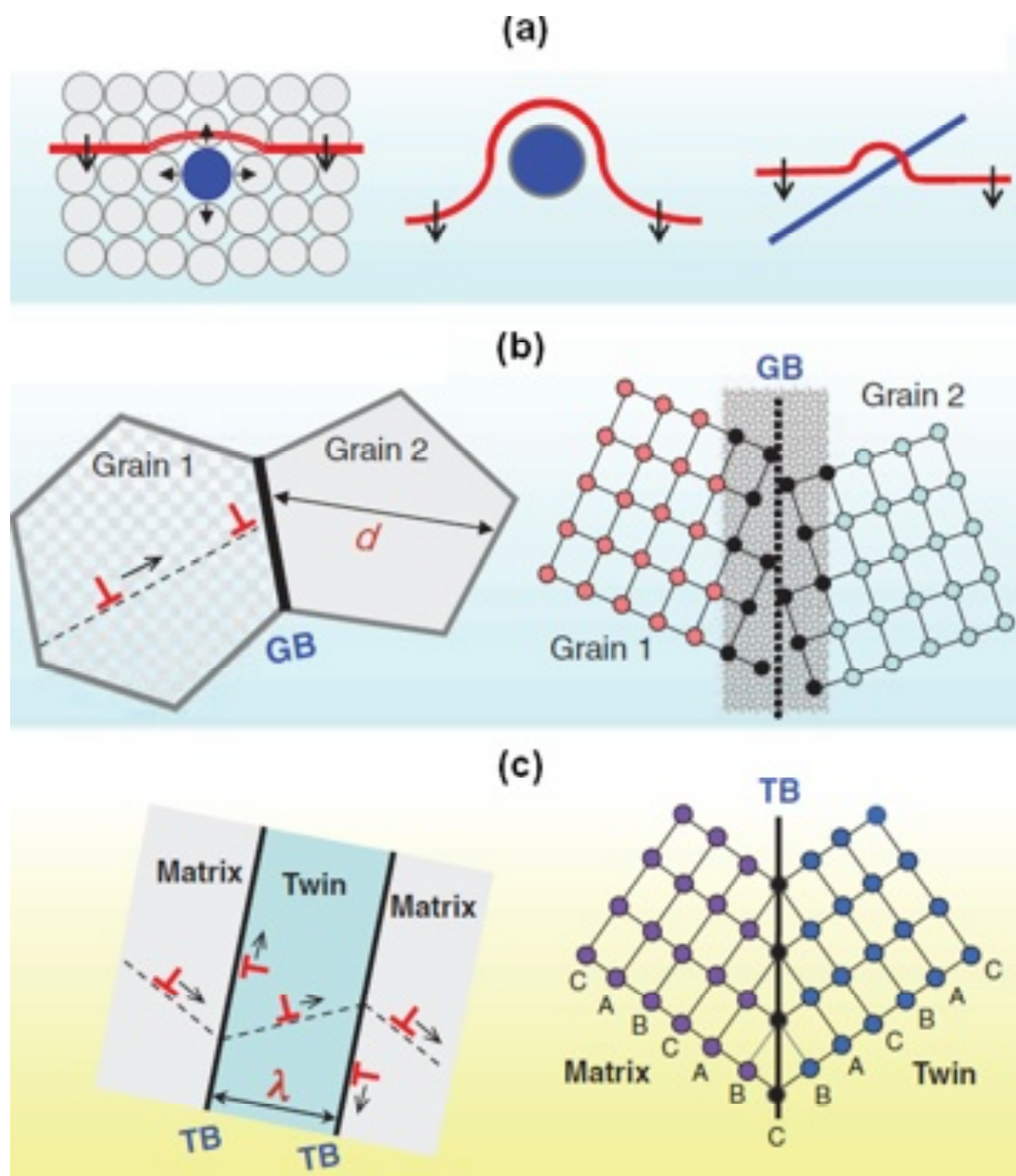


Fig. 9. Schematic illustration of different strengthening metals and alloys: (a) solid solution, solid nanoparticle and dislocation forest; (b) traditional grain boundary strengthening and (c) nanotwinning strengthening. Incoherent high-angle boundaries and coherent low-angle those are shown at (b) and (c), respectively (adapted from [16]).

on the coherent boundaries, and no non-glissile Frank dislocations ($b = 1/3[111]$) under dislocation dissociation reactions, such as

$$1/2[101] \rightarrow 1/6[1\bar{2}1] + 1/3[111].$$

It is believed that glissile Shockley partial dislocations provide plasticity and non-glissile Frank dis-

locations are responsible for the strength. The formation of Shockley partial dislocation is confirmed by the HRTEM results (Fig. 10, adapted from [2]). However, a comprehensive analysis of experimental data, results of the MD methods simulation and other techniques have shown [15,17] that some of the details of the dislocations interaction mecha-



Fig. 10. HRTEM image of the structure close to the failure of electrodeposited Cu sample C (Fig. 1c3) with Shockley partial dislocations at the nanotwinned boundaries (adapted from [2]).

nisms with nanotwins and their influence on the strength and ductility still require further investigation.

It was established experimentally that the decrease of the twin lamellae thickness leads to the increase of strength and ductility as well as to the increase of the coefficient of rate sensitivity $m = (\partial \ln \tau / \partial \ln \dot{\epsilon})$, where τ and $\dot{\epsilon}$ are the stress of deformation and strain rate, respectively. Fig. 11 demonstrates the influence of the value of d and λ on these characteristics for the electrodeposited copper samples (Figs. 1 and 2).

As can be seen from Figs. 11a and 11c, the influence of the of d and λ values on the strength and the rate sensitivity has as a whole a similar character. In contrast, the dependences of the elongation have the opposite forms (Fig. 11b), reflecting the significantly different nature of dislocation behavior, as can be seen also at Figs. 9b and 9c. The depen-

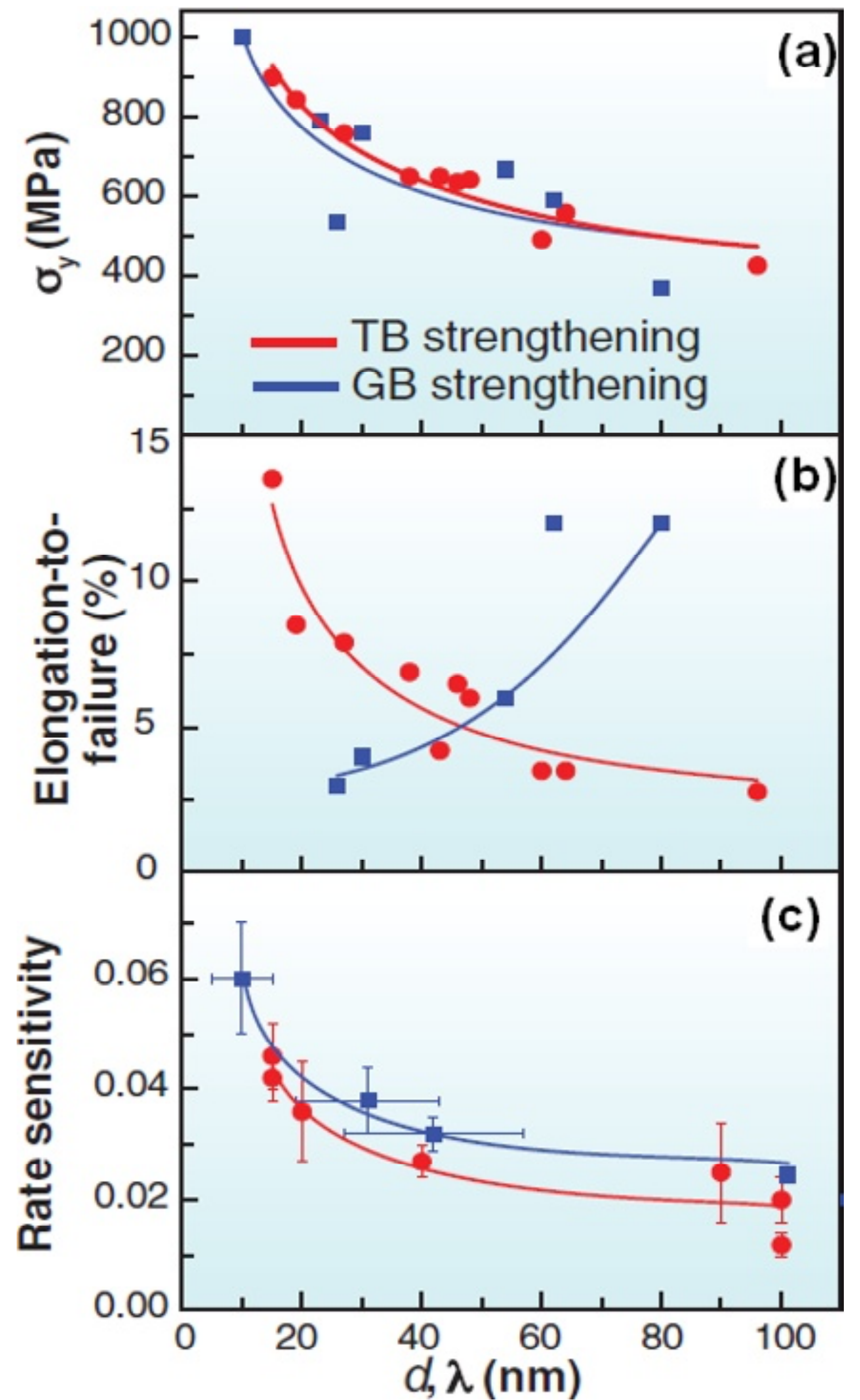


Fig. 11. Effect of grain size (d – blue lines, ■) and of twin lamellar thickness (λ – red lines, ●) on properties of nanomaterials: (a) strength/hardness, (b) elongation-to-fraction, and (c) rate sensitivity (adapted from [16]).

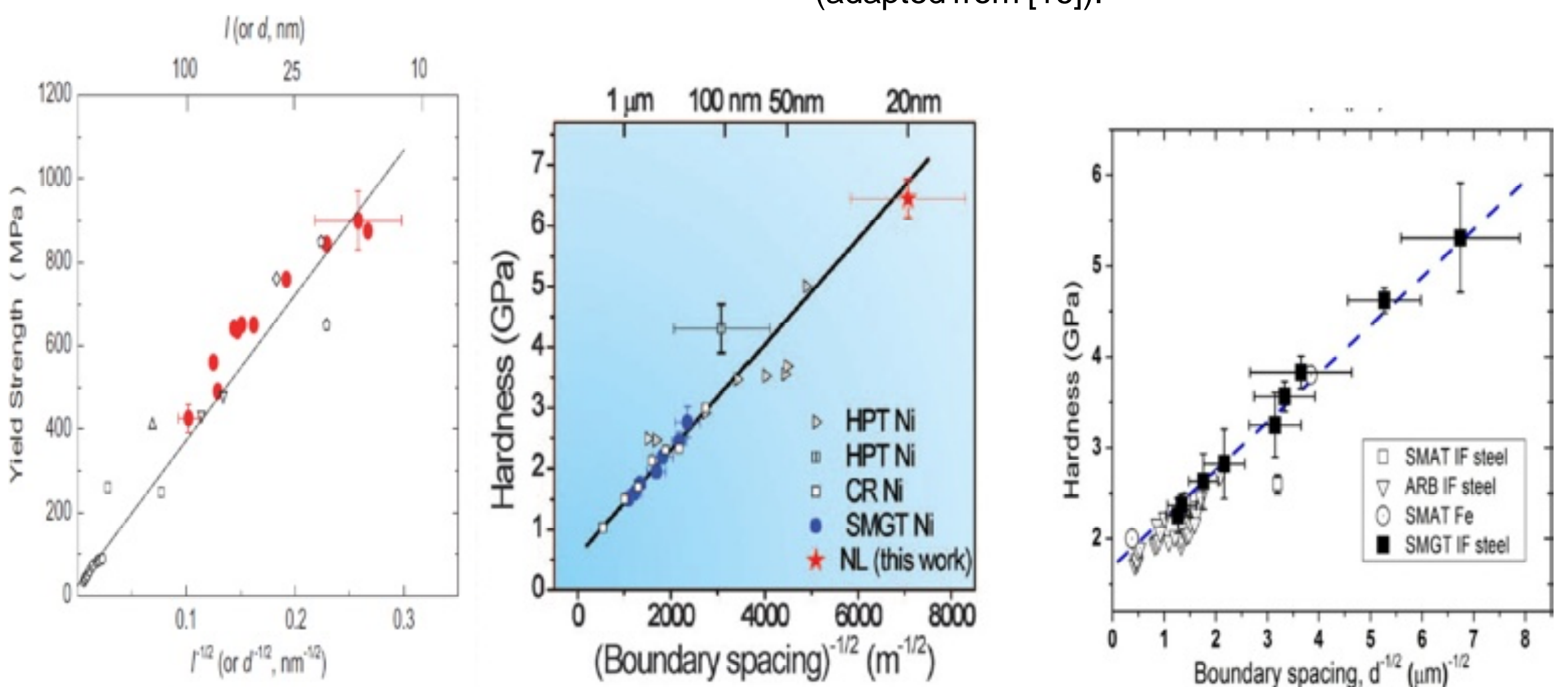


Fig. 12. Plots of tensile yield strength of Cu (a) as well as of hardness of Ni (b) and Fe (c) as a function of the boundary spacing for samples processed by different methods such as electrodeposition (Cu); high pressure torsion and surface mechanical grinding treatment (Ni); surface mechanical attrition treatment, accumulative roll-bonding and surface mechanical grinding treatment (Fe). NL is nanolaminated structure with the strongly textured twins (an average lamellar thickness about 20 nm); CR is coarse-grained Ni (adapted from [2,8,18]).

Table 2. Mechanical properties of Ti before and after different technology treatments (σ_{UTS} is an ultimate tensile stress, σ_Y is an yield stress, and δ is an elongation to fracture).

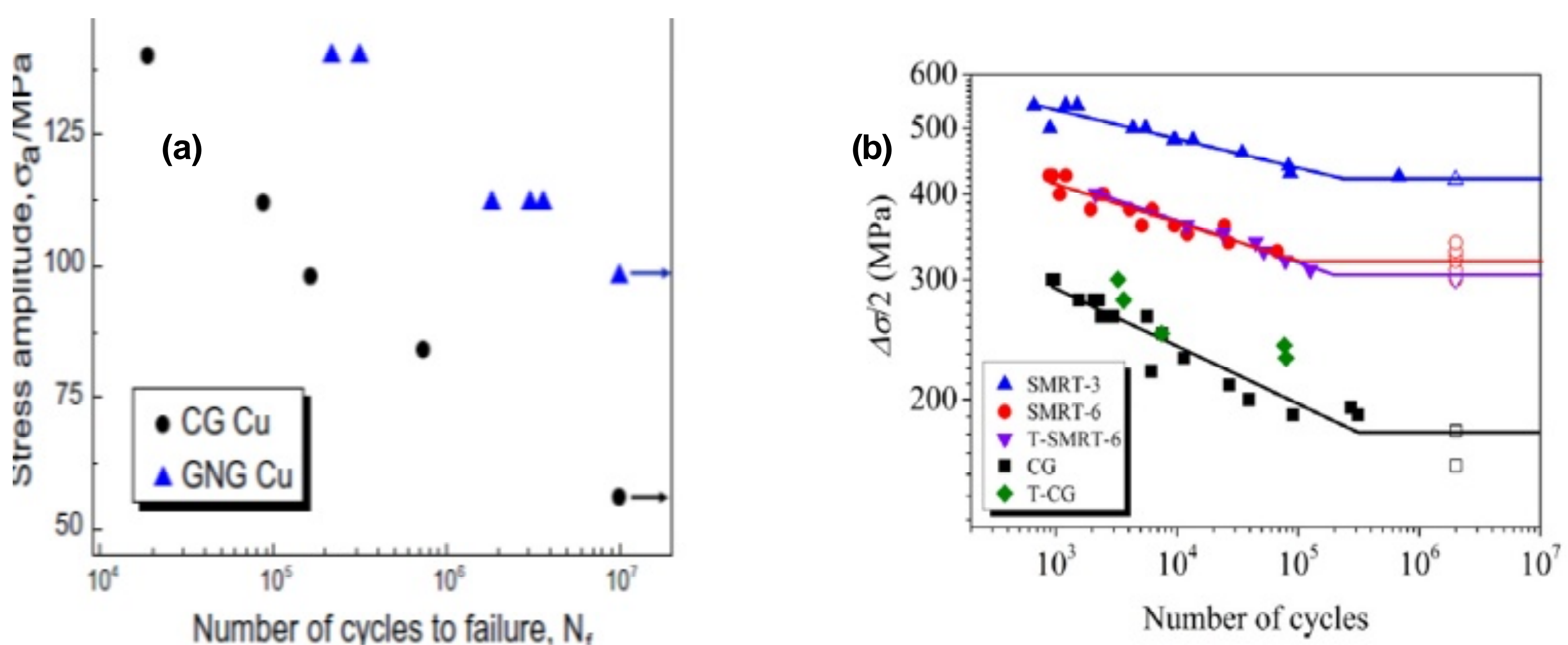
| Treatment | Sample | Grain size (nm) | σ_{UTS} (MPa) | σ_Y (MPa) | δ (%) |
|---|---------|-----------------|----------------------|------------------|--------------|
| SRT [9] | Initial | 3×10^4 | 451 | 380 | 24 |
| | Final | See Fig. 7 | 495 | 437 | 21 |
| ECAP [19] | Initial | 3×10^4 | 700 | 530 | 25 |
| | Final | ~ 200 | 1240–1250 | 1000–1250 | 11–13 |
| ARB at low temperatures [20] | Initial | n/d | 420 | 300 | 26 |
| | Final | 35–70 | 700– | 665–860 | 6–11 |
| Screw and sizing length-wise rolling [21] | Initial | n/d | 490 | 376 | 29 |
| | Final | 180–190 | 850–905 | 670–722 | 10–12.5 |

dences of hardness and strength on $d(\lambda)$ follow to a known ratio of the Hall-Petch relation which is demonstrated on the example of copper, nickel and iron in Fig. 12 (adapted from [2,8,18]).

It is believed that nanolaminated structures in the surface areas of Ni and Fe with the λ values of 10–20 nm are formed due to the large deformation gradient, which are accompanied by a significant dislocation activity and correspondingly high values of hardness superior to those for samples treated by conventional SPD methods [18]. It is interesting to stress that in initial iron samples of 10 mm diameter and grain size of about 27 μm , the content of high-angle boundaries was about 92% [18]. In this case, after the SMGT, the total length of the deformation zone was approximately 400 μm and a twin lamellae thickness less than 100 nm was observed at a distance from the surface to about 20 μm .

It should be noted that high values of hardness in samples, subjected by the SMAT, SMGT, and SRT deformation, are fixed only for the surface layer and the overall strength increase is not so high as compared with that of counterparts after usual methods of SPD and pulse electrodeposition. Table 2 summarizes the mechanical properties of the Ti samples in initial state and after different treatments.

As can be seen from these data, the increase in the overall mechanical properties as a result of nanostructuring in the case of the SRT is much lower than in the case with other methods of SPD due to the small length of the deformation zone. However, these samples with gradient structure have wholly satisfactory parameters of plasticity and, in addition, are characterized by a high resistance to cyclic fatigue actions. Fig. 13 shows the fatigue re-

**Fig. 13.** S–N curves of different samples of Cu (a) processed by SMGT (● CG is initial coarse-grained sample; ▲ GNG is gradient nanograined one) and AISI 316L stainless steel (b) processed by SMRT (■ CG is initial coarse-grained sample; ▲● are SMRT-3 and SMRT-6 samples with diameter 3 mm and 6 mm; ▲◆ are SMRT-6 and CG samples after an uniaxial tensile strain of 3%, respectively (adapted from [22,23]).

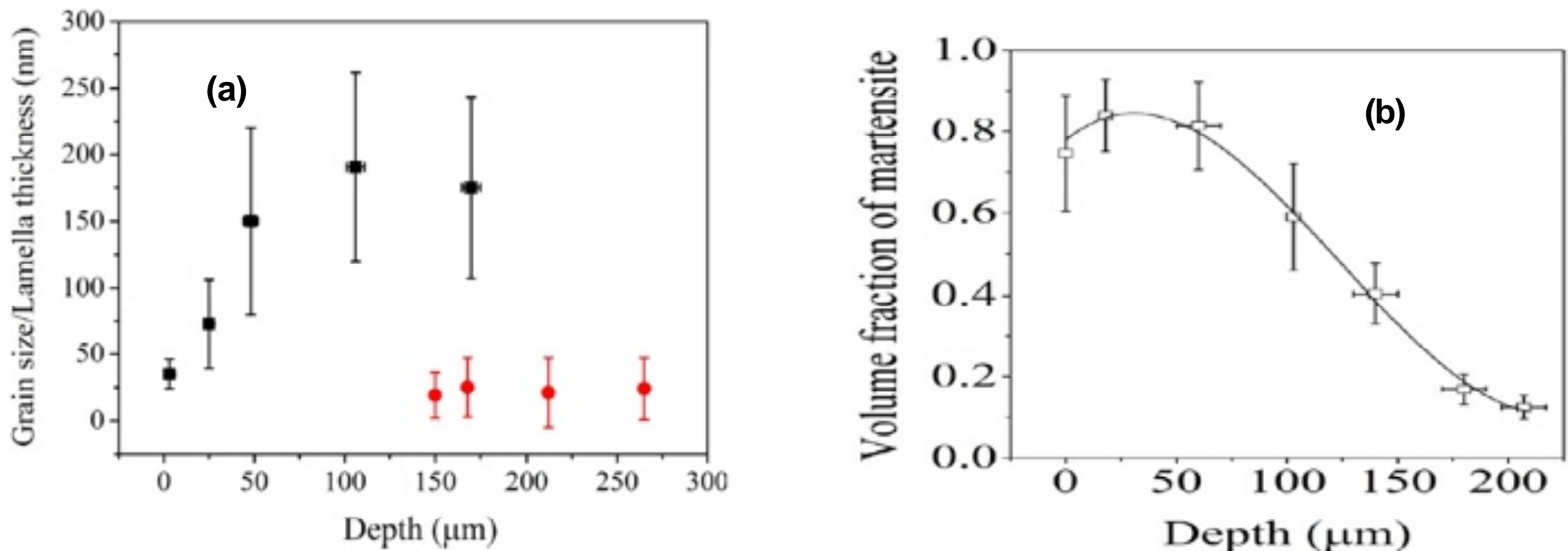


Fig. 14. (a) Grain size (■)/lamella thickness (●) and (b) volume fraction of martensite vs. depth in the SMRT 316L stainless steel sample (adapted from [23]).

sponse of copper and AISI 316L austenitic stainless steel with a gradient nanograined surface layer (adapted from [22,23]).

Fig. 13 shows the so-called Weller $S-N$ curves reflecting the effect of the number of cycles to failure at stress amplitude (Cu) and at half of the amplitude of the stress (316L). It is clearly seen that the surface deformation processing (such as SMGT and SMRT) significantly improves fatigue properties as compared with those for coarse-grained samples. It is important also that this improvement is observed both in the low- and in the high- cycling fatigue regimes. It is significant that, for example, in the case of conventional ultrafine-grained copper ($d \sim 200$ nm) processed by ECAP, the fatigue strength improvement was found to decrease markedly in the high-cycle fatigue range [24].

The most detailed study of the SMRT effect on the fatigue properties improvement has been performed as applied specially to the gradient nanostructured surface layer of AISI 316L stainless steel [23]. The following main results can be pointed: 1) The sample diameter decrease was found to be more effective in the fatigue strength enhancement than in the preliminary deformed samples (Fig. 13b). 2) Detailed microstructural characterization of the surface layers using TEM, XRD and selected area electron diffraction permitted to reveal some variations of d and λ values of martensite phase forming from the prior austenite one. Fig. 14 shows variations of grain size and twin lamellar thickness as well as of martensite phase content with depth in the SMRT sample.

As can be seen from Fig. 14, the nanosized martensite grains ($d < 100$ nm) formation begins from the top of 40 μm surface layer, and then these martensite grains are increasing with depth in the

top 100 μm up to 170 nm. In the subsurface layer (with a depth from 150 to 270 μm) the twin lamellar thickness of dominant austenite phase is about 25 nm.

3) The variations of microhardness with distance from treated surface and in-depth residual stress distributions are demonstrated in Fig. 15 (adapted from [23]). The data of Fig. 15a shows that the microhardness reaches a maximum value of ~ 5.5 GPa at the topmost surface and decreases gradually to the matrix value of about 1.8 GPa at a depth of ~ 1 mm. The maximum value of ~ 5.5 GPa is more than those in the case of other SPD actions and connected with both the grain refinement effects and higher concentration of martensite phase. Remarkable high compressive residual stresses at the topmost surface layers are fixed for both martensite and austenite phases (Fig. 15b), but they are relaxing under deformation and changed significantly because of their tensile character.

4) The detailed analysis of all obtained results, including the surface morphology studies, tends to the statement, that this high fatigue strength of the SMRT samples is explained by the absence of persistent slip bands or cracks on the surface during cyclic deformation, owing to the surface morphologies remain unchanged even after 1.8×10^5 cycles. The gradient nanostructured surface layers improve the material fatigue properties due to a suppression the cracks initiation of and accommodation of a considerable cyclic plastic strain amplitude by reducing strain localization. The effect of the remarkable compressive residual stresses is insignificant. It was also found that the general tensile strength increase in the case of the SMRT 316L samples is not so high, compared to counterparts processed by the ECAP, likely to the Ti samples (Table 2).

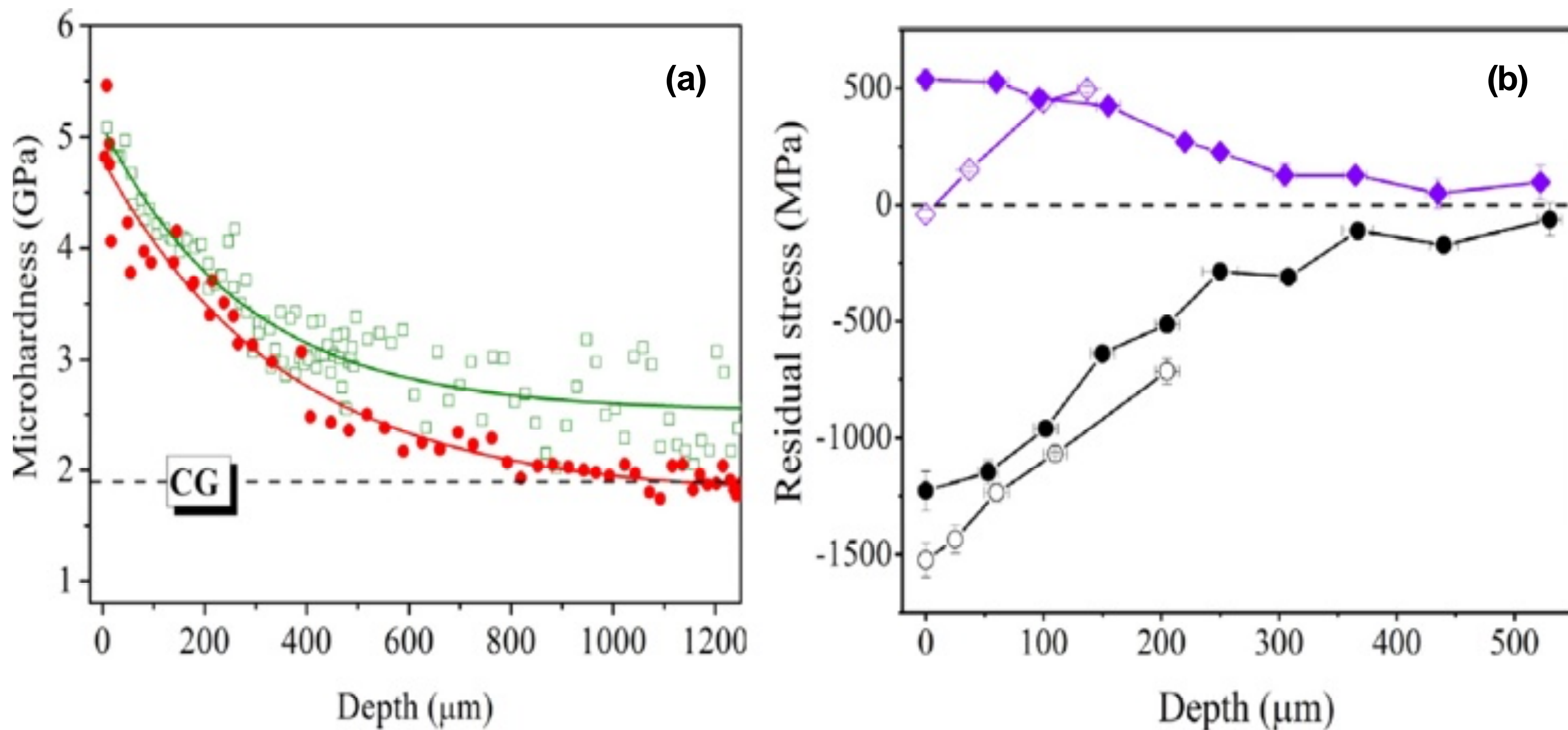


Fig. 15. (a) The microhardness value of 316L stainless steel as function of distance from treated surface of the as-SMRT sample (●) and the SMRT one after fatigue at $\Delta\sigma/2 = 325$ MPa (□) and (b) in-depth residual stresses distributions in martensite (○◇) and austenite (●◆) phases for the as-SMRT samples (○●) and those after an uniaxial tension strain of 3% (◇◆), respectively (adapted from [23]).

It is of interest to note the influence of nanotwinned structures in the improvement of the mechanical and physical and chemical properties in the case of classical superhard materials-based cubic boron nitride and diamond. Table 3 provides information about the microhardness (H_V), fracture toughness (K_{IC}) and the temperature of the beginning of oxidation (T_{oxid}) for nanocrystalline and nanotwinned samples of cubic boron nitride (cBN) and diamond [25,26].

Samples c-BN and diamond with nanotwinned structure were obtained by the method of high pressures and high temperatures ($P = 10\text{--}25$ GPa and $T = 1800\text{--}2000$ °C) using the original nanoparticles with primary onion-like structures [25,26]. As can be seen from Table 3, the advantages of nanotwinned structures are quite obvious. Fig. 16 shows the features of the nanostructure of cubic boron nitride,

the twin lamellar thickness distribution and the effect of the values of $\lambda(d)$ on hardness (adapted from [25]). In many respects, the data shown in Fig. 16 are similar to the earlier mentioned analogous results for metallic nanomaterials, but the improvement of characteristics, such as H_V , K_{IC} , and T_{oxid} , has yet to be clarified in further research as applied to superhard brittle materials.

Undoubtedly, the most important feature of the nanotwinned materials is connected with the high electrical properties, being very close to their coarse-grained counterparts. Fig. 17 shows the temperature dependence of resistivity for the copper samples having different structure.

These data indicate that the values of electrical resistivity at 293K and below are very near for both coarse-grained and nanotwinned samples, because for these objects the main contributions to the elec-

Table 3. Properties of nanotwinned/nanocrystalline cubic BN [25] and diamond [26].

| Subject | Structure characteristics | | H_V (GPa) | K_{IC} (MPa m ^{1/2}) | T_{oxid} (°C) |
|-------------------------|---------------------------|------------------------------|-------------|----------------------------------|-----------------|
| | Grain size (nm) | Twin lamellar thickness (nm) | | | |
| Nanocrystalline c-BN | ~ 14 | — | 85 | 6.8 | ~ 1100 |
| Nanotwinned c-BN | — | 3.8 | ~ 110 | 12.7 | ~ 1300 |
| Nanocrystalline Diamond | 10–30 | — | 110–140 | 5–15 | ~ 800 |
| Nanotwinned Diamond | — | ~ 5 | 175–204 | 9.7–14.8 | ~ 1000 |

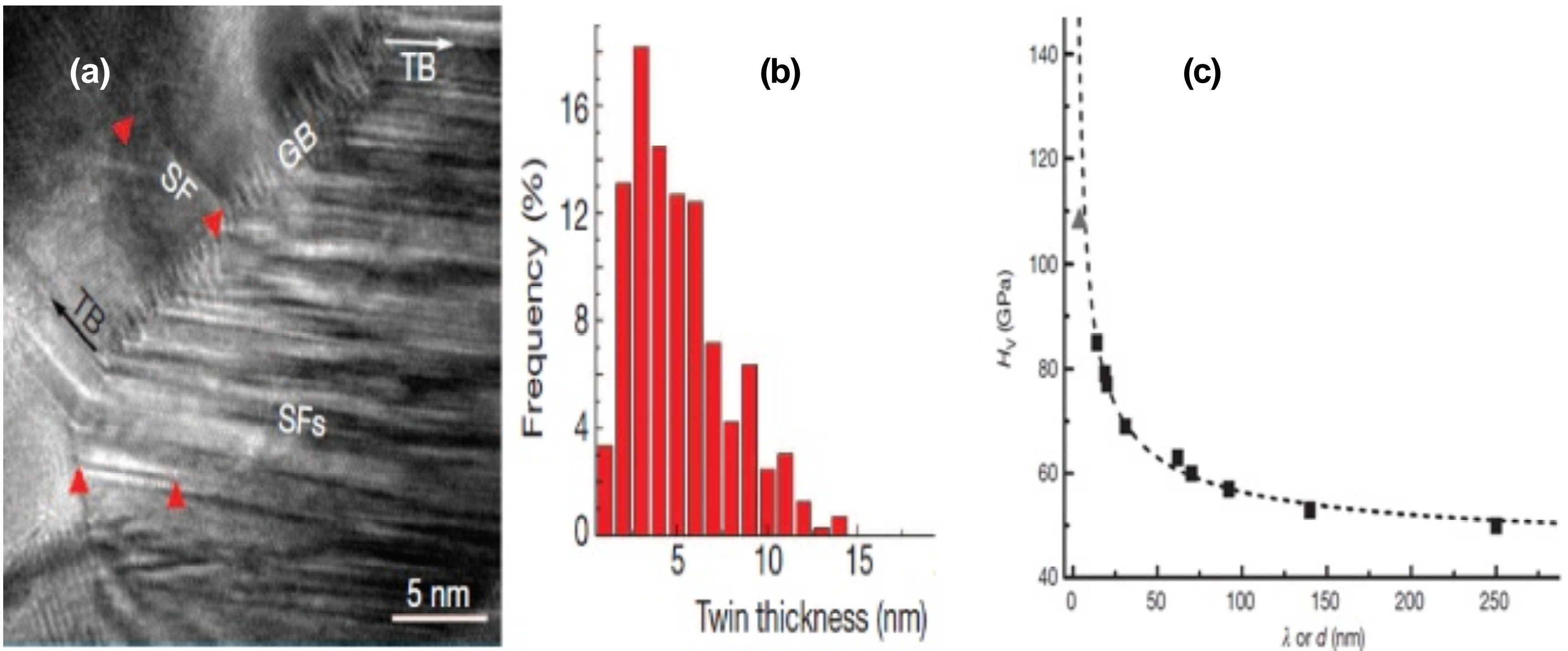


Fig. 16. (a) HRTEM image of nanotwinned cBN showing Shockley partial dislocations (red triangles) emitted from grain boundaries (GB) and a high density of stacking faults (SF) in twin domains. (b) Thickness distribution of the twins with an average twin thickness of 3.8 nm. (c) A Vickers hardness (H_V) as a function of average grain size (\blacksquare is d) or twin lamellar thickness (\blacktriangle is λ) for polycrystalline cBN bulk materials (adapted from [25]).

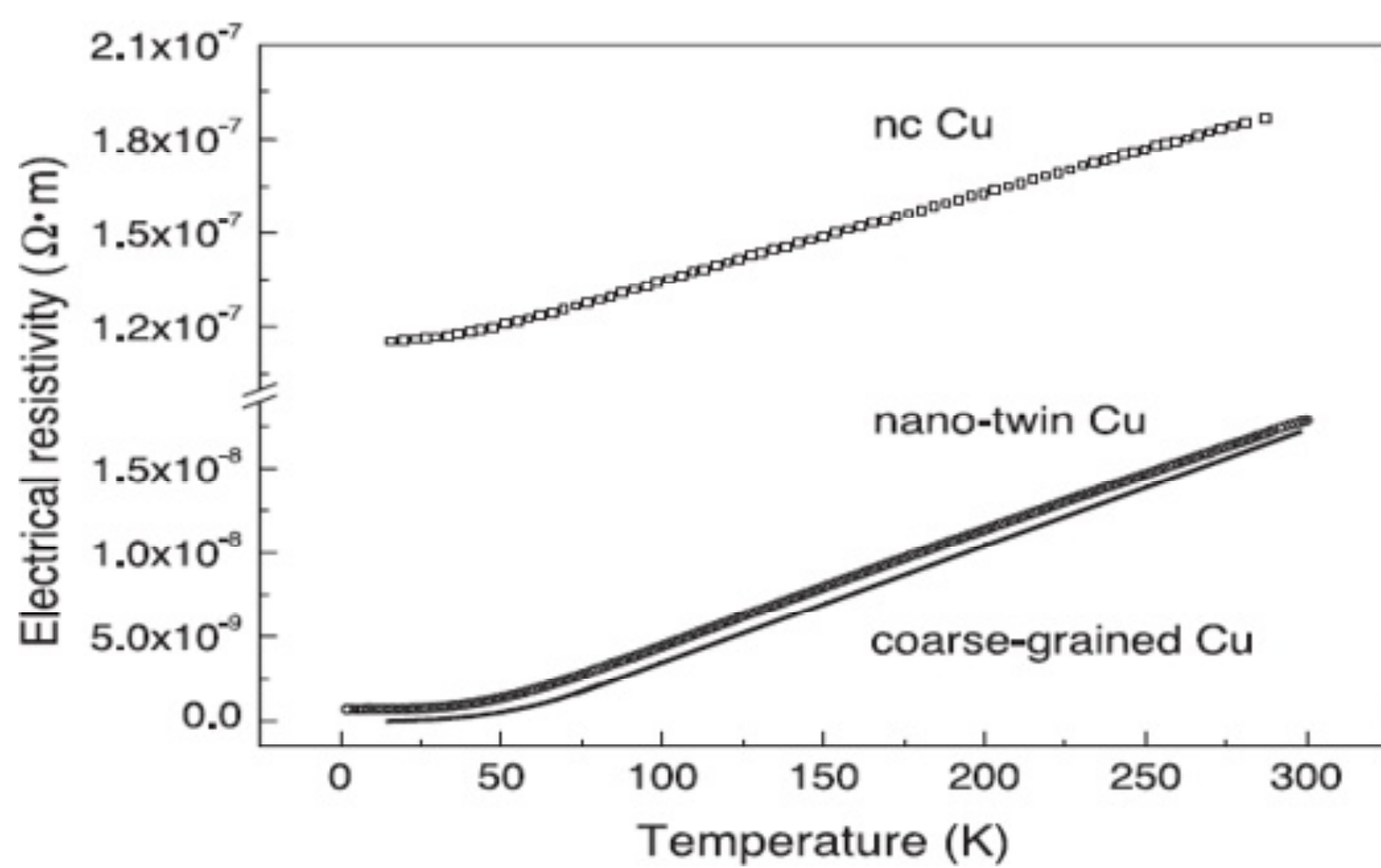


Fig. 17. The temperature dependence of electrical resistivity for the as-deposited nanotwinned Cu sample as well as coarse-grained one and nanocrystalline one (nc; with a mean grain size of 15 nm) (adapted from [1]).

tron scattering can be attributed to atomic thermal vibrations and impurities. Electron scattering on crystal defects, such as dislocations and grain boundaries, plays a significant role only in the case of nanocrystalline samples (nc Cu). Simple evaluation also showed that the resistivity of small-angle twinned boundaries is almost two times lower than that for conventional high-angle boundaries. The low resistivity of nanomaterials with nanotwinned structure (in combination with high strength and good plasticity) opens wide prospects for their use in electrical engineering. In that respect, the example of polyfunctional nanocomposite Cu/Nb wire is very indicative [27,28]. Such wire usage in solenoids allows create the super strong (>60 T) magnetic field pulses with following parameters: strength not be-

low 1 GPa (for to resist to a great Lorenz force arising in magnetic fields); electrical conductivity not below 0.6 of the value for pure copper (for the ohmic losses minimization); operational temperature in 77–673K range; fatigue durability over 5000 cycles; the radiation stability up to He ions flow densities above 10^{15} ions/cm². The material structure (Cu matrix with about 21 vol.% Nb nanotubes, diameter of ~ 140 nm) meeting these tough demands was created by a complex SPD treatment, including repeated hot extrusion/rolling processing, cold drawing, and bundling cycles.

3.2. Thermal and irradiation stability

Fig. 3 has already demonstrated the stable behavior of columnar nanotwinned Cu structure. The temperature effect on the hardness and the grain size/twin lamellar thickness of Cu samples [3] and the temperature change of λ of Ni samples [8] are shown in Fig. 18. As follows from Fig. 18, compared with conventional nanomaterials, the advantage of nanotwinned copper and nanolaminated nickel is quite obvious, and it can be clearly associated with low grain boundary energy and small mobility of small-angle boundaries, as well as the influence of the columnar shape of the lamellae [3,8,29]. Coherent nanotwinned boundaries are characterized by much lower stored energy than conventional high-angle grain boundaries, and hence have a significantly reduced driving force for the coursing of twins [29].

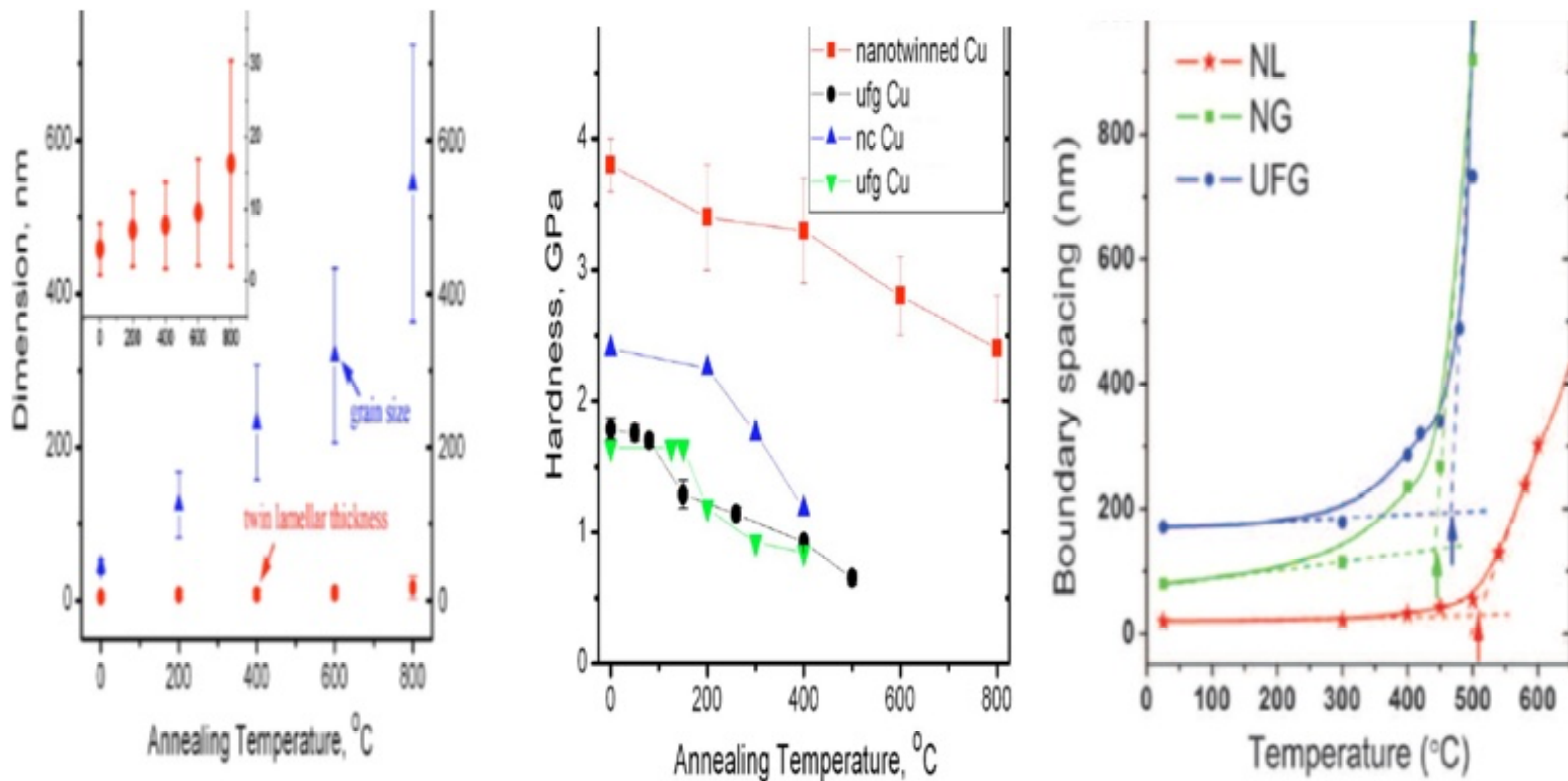


Fig. 18. Effect of annealing temperature on grain size and twin lamellar thickness (a) and hardness (b) of Cu samples as well as on boundary spacing of Ni those (c). UFG is ultrafine-grained sample ($d \sim 200$ nm); NC and NG are nanocrystalline and nanograined those; NL is nanolaminated sample ($h \sim 20$ nm). The inset in (a) shows the average lamellar thickness as a function of temperature clearly. The arrows in (c) indicate the onset temperatures for obvious grain coarsening which for NL sample, NG one and UFG one are of ~ 506 °C, ~ 443 °C, and ~ 467 °C, respectively (adapted from [3,8]).

As was mentioned earlier, nanotwinned structure in Cu/Nb multilayer nanocomposites (Fig. 8) is also characterized not only by a high thermal resistivity (remaining stable with no signs of violations during annealing up to 500 °C [14, 30]), but also by a high resistance with reference to the extreme plastic deformation and ion irradiation. Nanolaminated layered structures (with thickness of individual layers about 20 nm) remain stable after great plastic strains, and a formation of pores and dislocation defects was not detected in these materials after the He ion irradiation [30]. Positive effect of nanotwinned structure on the irradiation stability increase has been observed in many other studies related to metals (Ag, Cu, and Nb) as well as SiC (e.g., [31-37]). In these cases, numerous twin boundaries are effective sinks for radiation defects type of stacking fault tetrahedra (vacancy clusters), that was experimentally shown for Ag nanotwinned films irradiated by Kr ions [31,32]. The radiation defects absorption was fixed using *in situ* TEM examination of coherent $\Sigma 3\{111\}$ and incoherent $\Sigma 3\{112\}$ twin boundaries including their migration. The comparison of the behavior of the nanocrystalline Cu and nanolaminated Cu/Nb samples under He irradiation revealed that the heterophase interfaces facilitate the removal of radiation defects much more [35].

The study of irradiated nanostructured films-based wide band gap semiconductor β -SiC has also identified that objects with a high density of planar defects in the form of stacking faults and twins are more resistant to amorphization compared to single crystal SiC [36,37]. The presence of these layers significantly enhanced recombination of interstitials and vacancies, leading to self-healing irradiation-induced defects and increasing resistance to amorphization.

3.3. Corrosion action

From a general view point, the presence of large numbers of interfaces, on one hand, must have an affect on the materials corrosion performance, because these sites (with their disordered structure) are subjected to selective interactions with an aggressive media. On the other hand, the diffusion-controlled formation of the protective surface films (that is, surface passivation) at these interfaces can proceed more intensive, and this fact can prevent the further spread of corrosion. General effect for the many material interaction with an environment can be determined by relation of these two factors and depends on reaction parameters (their kinetic rate constants) as well as on the nanostructure parameters. In this situation, the nanomaterials can

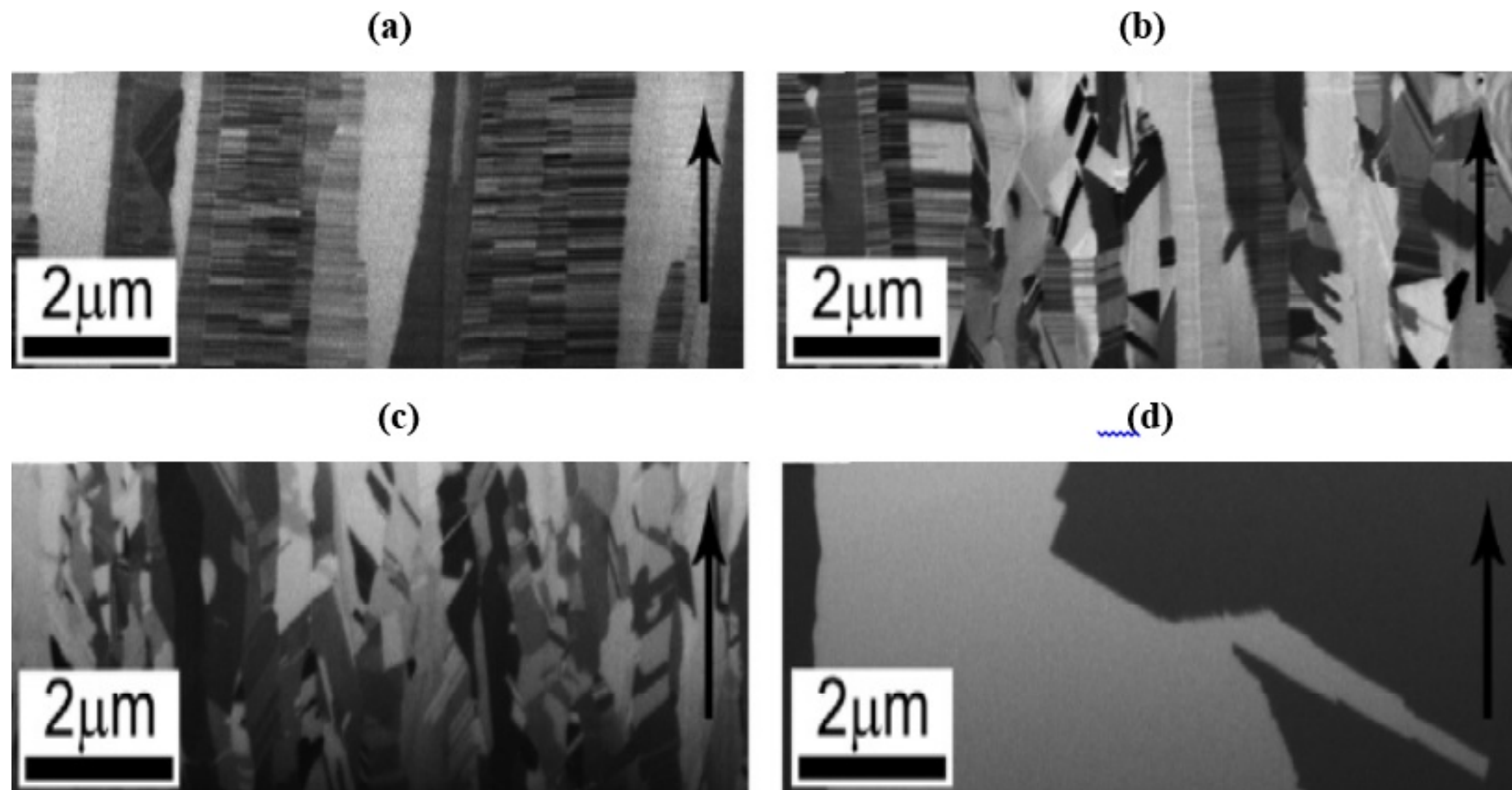


Fig. 19. Focused ion beam cross-sectional micrographs of Cu foils: (a) as-prepared with highly nanotwins; (b) partially those; (c) non those; (d) microcrystalline samples (adapted from [45]).

be both more or less corrosion-resistant in comparison with their coarse-grained counterparts, and this non-trivial situation has led to many conflicting results, related to the nanomaterials corrosive and electrochemical behavior, as was especially noted in recent reviews [38-42].

The opposite effect of grain size on oxidation of Fe–Cr alloys and pure Ni has been observed in the case of micro- and nanocrystalline samples [41,43,44]. Oxidation of nanocrystalline Fe–10Cr sample was accompanied by intensive formation of dense protective Cr_2O_3 film due to an increased Cr diffusion mobility in nanograins and this is favorable to the decrease of oxidation rate in nanoalloys. For the nanocrystalline nickel samples, it was demonstrated that the accelerated NiO film formation is also explainable with Ni boundary diffusion but this film is not a passivating one and microcrystalline samples are oxidized in smaller degree as compared with nanocrystalline counterparts.

As far as we know, the effect of nanotwins on corrosion properties of nanomaterials was studied

only in several works. The most detailed investigation was performed for Cu foil corrosion in artificial sea water (3.4% NaCl, pH ~ 8.0) [44]. A structure of investigated high-purity Cu (99.999%) samples prepared by magnetron sputtering is shown in Fig. 19 and results of corrosion tests are demonstrated in Table 4.

The data of Table 4 clearly shows that the greatest corrosion resistance have a film with a high concentration nanotwinned grain boundaries and the fraction of (111) texture (Fig. 19a), although the current density of passivation is approximately the same for all objects. The study of the protective passivation layer, including both electrochemical and immersion corrosion tests, showed the presence of columnar Cu_2O crystals with (111) texture, and the pitting smaller presence was found in films with the highest number of nanotwins (Fig. 19a). It is also interesting that, despite the great difference in the grain size (by more than an order of magnitude), corrosion characteristics of films *c* and *d* differed very little, that means, that the effect of grain size

Table 4. Summary of corrosion tests of nanotwinned and microcrystalline Cu foils with common thickness of ~ 25 μm (adapted from [45]).

| Designation in Fig. 19 | Grain size (μm) | % of grains with nano-twins | Area fraction of grains of (111) orientation | Polarization resistance ($\text{k}\Omega \text{ cm}^2$) | Corrosion current density ($\mu\text{A cm}^{-2}$) | Passivation current density (mA cm^{-2}) |
|------------------------|------------------------------|-----------------------------|--|---|---|---|
| <i>a</i> | 0.52 | 90 | 0.88 | 28.6 ± 7.1 | 0.34 ± 0.09 | 1.15 ± 0.20 |
| <i>b</i> | 0.41 | 60 | 0.33 | 10.2 ± 4.4 | 1.08 ± 0.39 | 1.14 ± 0.23 |
| <i>c</i> | 0.34 | 5 | 0.08 | 10.4 ± 0.5 | 1.26 ± 0.06 | 1.08 ± 0.27 |
| <i>d</i> | 8.6 | 0 | 0.02 | 9.2 ± 2.1 | 1.92 ± 0.42 | 1.27 ± 0.18 |

was not the determining factor in results [45] and the main contribution to the change in corrosion resistance made namely notwinned structures.

3.4. Some theoretical approaches and modeling

In the main, the above mentioned examples of the nanotwinned structure impact on the nanomaterials properties included the experimental results. It should be noted in short that a sufficient number of theoretical approaches and MD simulation including a multi-scale version (see, for example, only some recent studies [46-56]). The following situations have been examined in these papers:

- the dislocation nucleation governed strength-softening regimes in nanotwinned Cu [46];
- the effect of $\Sigma 3$ twin low-angle boundaries on the formation of radiation-induced defect clusters in nanotwinned Cu [47];
- an universal scaling law of planar fault energy barriers in FCC metals [48];
- mechanisms of energy minimization for semi-coherent interfaces [49];
- different theoretical models describing plastic deformation and fracture processes in ultrafine-grain and nanocrystalline metallic nanomaterials [50-53];
- MD simulation of the mechanical properties of crystalline/crystalline and crystalline/ amorphous nanolayered objects [54];
- MD simulation of the fracture behavior of twinned Cu nanowires including cases of ductile and brittle fracture as well as ductile-to-brittle transition [55];
- an atomic scale view of change of the crack-tip events from crack cleavage to dislocation activity in nanotwinned FCC crystals under low temperatures [56].

However, a detailed analysis of these data with comparison of numerous experimental results is beyond the scope of our overview and requires separate consideration.

4. CONCLUSIONS

As follows from the above, twinned structures play a big role in the properties of metallic nanomaterials. It should be also noted the significant information about high-strength steels with transformation-induced plasticity (TRIP) and twinned-induced plasticity (TWIP) (e.g., [57,58]), which in our review were not considered. Discussion of the twins features is found to spread and apply in other types of materials, in particular titanates and aluminates (e.g.,

[59]). The presence of twins makes nanomaterials tolerant to almost many extreme conditions, associated with high temperatures as well as with irradiation, deformation and corrosion actions or their combined influence. Nevertheless, existing data on high temperature creep, high-cycle fatigue, high irradiation doses, and different corrosion actions are needed for significant enlargement. Of course, the continuous progress of modern technique demands also stimulates and requires additional experimental and theoretical studies, especially in synergetic effects and forecasting capabilities.

The gradient/lamellar structure perspectives are highlighted in many recent publications (e.g., [60-63]). In addition, some new their producing routes, such as laser shock peening, ultrasonic nanocrystal surface modification, formation of twins during primary recrystallization, mixed carbide synthesis, nanolaminate Ti_3SiC_2 -based material prepared by self-propagating high-temperature synthesis, and so on are appearing (e.g., [64-68]). In line with this, the comparison of different methods for producing effective nanomaterials tolerating different extremes seems to be very important and urgent.

ACKNOWLEDGEMENTS

The author is grateful to V.V. and S.V. Klyucharev for their effective help in the manuscript preparation. Financial support from the Russian Basic Research Foundation and the Russian Academy of Sciences is also appreciated.

REFERENCES

- [1] L. Lu, Y. Shen, X. Chen, L. Qian and K. Lu // *Science* **304** (2004) 422.
- [2] Y.F. Shen, L. Lu, Q.H. Lu, Z.H. Jin and K. Lu // *Scr. Mater.* **52** (2005) 989.
- [3] O. Anderoglu, A. Misra, H. Wang and X. Zhang // *J. Appl. Phys.* **103** (2008) 94322.
- [4] R. Andrievski // *J. Mater. Sci.* **49** (2014) 1449,
- [5] L. Lu, X. Chen, X. Huang and K. Lu // *Science* **323** (2009) 607.
- [6] K.Y. Yu, D. Bufford, Y. Chen, Y. Liu, H. Wang and X. Zhang // *Appl. Phys. Lett.* **103** (2013) 181903.
- [7] Y. Estrin and A. Vinogradov // *Acta Mater.* **61** (2013) 782.
- [8] X.C. Liu, H.W. Zhang and K. Lu // *Science* **342** (2013) 337.
- [9] Q. Wang, Y. Yin, Q. Sun, L. Xiao and J. Sun // *J. Mater. Res.* **29** (2014) 569.
- [10] Y.T. Zhu, X.Z. Liao and X.L. Wu // *Progress Mater. Sci.* **57** (2012) 1.

- [11] X.L. Wu and E. Ma // *Mater. Sci. Eng. A* **483–484** (2008) 84.
- [12] X.L. Wu and Y.T. Zhu // *Phys. Rev. Lett.* **101** (2008) 025503.
- [13] Y. Li, Y.H. Zhao, W. Liu, C. Xu, Z. Horita, X.Z. Liao, Y.T. Zhu, T.G. Langdon and E.J. Lavernia // *Mater. Sci. Eng. A* **527** (2010) 3942.
- [14] I.J. Beyerlein, A. Caro, M.J. Demkowicz, N.A. Mara, A. Misra and B.P. Uberuaga // *Mater. Today* **16** (2013) 443.
- [15] M. Dao, L. Lu, R.J. Asaro, J.T.M. De Hosson and E. Ma // *Acta Mater.* **55** (2007) 4041.
- [16] K. Lu, L. Lu and S. Suresh // *Science* **324** (2009) 349.
- [17] T. Zhu and H. Gao // *Scr. Mater.* **66** (2012) 843.
- [18] X.C. Liu, H.W. Zhang and K. Lu // *Scr. Mater.* **95** (2015) 54.
- [19] I.P. Semenova, G.Kh. Salimgareeva, V.V. Latysh, T. Lowe and R.Z. Valiev // *Mater. Sci. Eng. A* **503** (2009) 92.
- [20] V.A. Moskalenko, V.I. Betekhtin, B.K. Kardashev, A.G. Kadomtsev, A.R. Smirnov, R.V. Smolyanets and M.V. Narykova // *Phys. Sol. State* **56** (2014) 1590.
- [21] V.I. Betekhtin, Yu.R. Kolobov, V. Sklenicka, B.K. Kardashev and I.N. Kuz'menko // *Techn. Phys.* **60** (2015) 66.
- [22] L. Yang, N.R. Tao, K. Lu and L. Lu // *Scr. Mater.* **68** (2013) 801.
- [23] H.W. Huang, Z.B. Wang, J. Lu and K. Lu // *Acta Mater.* **87** (2015) 150.
- [24] R.H. Li, Z.J. Zhang, P. Zhang and Z.F. Zhang // *Acta Mater.* **61** (2013) 5857.
- [25] Y. Tian, B. Xu, D. Yu, Y. Ma, Y. Wang, Y. Jiang, W. Hu, Ch. Tang, Y. Gao, K. Luo, Zh. Zhao, L.-M. Wang, B. Wen, J. He and Zh. Liu // *Nature* **493** (2013) 385.
- [26] Q. Huang, D. Yu, B. Hu, W. Hu, Y. Ma, Y. Wang, Zh. Zhao, B. Wen, J. He, Zh. Liu and Y. Tian // *Nature* **510** (2014) 250.
- [27] A. Misra and L. Thilly // *MRS Bull.* **35** (2010) 965.
- [28] J.-B. Dubois, L. Thilly, P.-O. Renault and F. Lecouturier // *Adv. Eng. Mater.* **14** (2012) 998.
- [29] X. Zhang and A. Misra // *Scr. Mater.* **66** (2012) 860.
- [30] I.J. Beyerlein, J.R. Mayeur, S. Zheng, N.A. Mara, J. Wang and A. Misra // *Proc. NAS* **111** (2014) 4386.
- [31] K.Y. Yu, D. Bufford, C. Sun, Y. Liu, H. Wang, M. Li and X. Zhang // *Nature Comm.* **4** (2013) 1377.
- [32] K.Y. Yu, D. Bufford, F. Khatkhatay, H. Wang, M.A. Kirk and X. Zhang // *Scr. Mater.* **69** (2013) 385.
- [33] Y. Chen, K.Y. Yu, Y. Liu, S. Shao, H. Wang, M.A. Kirk, J. Wang and X. Zhang // *Nature Comm.* **6** (2015) 7036.
- [34] J. Li, K.Y. Yu, Y. Chen, M. Song, H. Wang, M.A. Kirk, M. Li and X. Zhang // *Nano Lett.* **15** (2015) 2922.
- [35] W. Han, M.J. Demkowicz, N.A. Mara, E. Fu, S. Sinha, A.D. Rollett, Y. Wang, J.S. Carpenter, I.J. Beyerlein and A. Misra // *Adv. Mater.* **25** (2013) 6975.
- [36] Y. Zhang, M. Ishimaru, T. Varga, T. Oda, Ch. Hardiman, H. Xue, Y. Katoh, S. Shannon and W.J. Weber // *Phys. Chem. Chem. Phys.* **14** (2012) 13429.
- [37] M. Ishimaru, Y. Zhang, S. Shannon and W.J. Weber // *Appl. Phys. Lett.* **103** (2013) 033104.
- [38] K.D. Raiston and N. Birbilis // *Corrosion* **66** (2010) 0750005.
- [39] L. Liu, Y. Li and F. Wang // *J. Mater. Sci. Technol.* **26** (2010) 1.
- [40] V. Maurice and Ph. Marcus // *Electrochim. Acta* **84** (2012) 129.
- [41] R.A. Andrievski // *Prot. Metals Phys. Chem. Surf.* **49** (2013) 528.
- [42] B.V. Mahesh and R.K. Singh Raman // *Metall. Mater. Trans. A* **45** (2014) 5799.
- [43] R.K. Gupta, R.K. Singh Raman and C.C. Koch // *J. Mater. Sci.* **45** (2010) 4884.
- [44] A.M. Rashidi // *Surf. Coat. Technol.* **205** (2011) 4117.
- [45] Y. Zhao, I.C. Cheng, M.E. Kassner and A.M. Hodge // *Acta Mater.* **67** (2014) 181.
- [46] X. Li, Y. Wei, L. Lu, K. Lu and H. Gao // *Nature* **464** (2010) 877.
- [47] M.J. Demkowicz, O. Anderoglu, X. Zhang and A. Misra // *J. Mater. Res.* **26** (2011) 1666.
- [48] Z.H. Jin, S.T. Dunham, H. Gleiter, H. Hahn and P. Gumbsch // *Scr. Mater.* **64** (2011) 605.
- [49] Sh. Shao, J. Wang and A. Misra // *J. Appl. Phys.* **116** (2014) 023508.
- [50] N.F. Morozov, I.A. Ovid'ko and N.F. Skiba // *Rev. Adv. Mater. Sci.* **37** (2014) 29.
- [51] S.V. Bobylev, H.F. Morozov and I.A. Ovid'ko // *Rev. Adv. Mater. Sci.* **41** (2015) 1.
- [52] S.V. Bobylev and I.A. Ovid'ko // *Rev. Adv. Mater. Sci.* **41** (2015) 20.

- [53] I.A. Ovid'ko, N.V. Skiba and A.G. Sheinerman // *Rev. Adv. Mater. Sci.* **41** (2015) 93.
- [54] X. Zhou and Ch. Chen // *Comp. Mater. Sci.* **101** (2015) 194.
- [55] J. Sun, L. Fang, A. Ma, J. Jiang, Y. Han, H. Chen and J. Han // *Mater. Sci. Eng. A* **634** (2015) 86.
- [56] L. Pei, Ch. Lu, K. Tieu, X. Zhao, L. Zhang, K. Cheng and G. Michal // *Mater. Lett.* **152** (2015) 65.
- [57] P. Xie, C.L. Wu, Y. Chen, J.H. Cen, X.B. Yang, S.Y. Duan, N. Yan, X.A. Zhang and J.Y. Fang // *Mater. Des.* **80** (2015) 144.
- [58] A. Weidner and H. Biermann // *JOM*, DOI: 10.1007/s11837-015-1456-y.
- [59] H. Wu, L. Li, L.-Zh. Liang, S. Liang, Y.-Y. Zhu and X.-H. Zhu // *J. Eur. Cer. Soc.* **35** (2015) 411.
- [60] K. Lu // *Science* **345** (2014) 1455.
- [61] X.L. Wu, P. Jang, L. Chen, J.F. Zhang, F.P. Yuan and Y.T. Zhu // *Mater. Res. Lett.* **2** (2014) 185.
- [62] X.L. Wu, P. Jang, L. Chen, F. Yuan and Y.T. Zhu // *PNAS* **111** (2014) 7197.
- [63] T. Ma, P. Hedström, V. Ström, A. Masood, I. Borgh, A. Blomqvist and J. Odqvist // *Int. J. Refr. Met. Hard Mater.* **51** (2015) 25.
- [64] Ch. Ye, Y. Liao, S. Suslov, D. Lin, G.J. Cheng // *Mater. Sci. Eng. A* **609** (2014) 195.
- [65] Ch. Ye, A. Talang, A.S. Gill, S. Suslov, Y. Idell, K. Zweiacker, J.M.K. Wiezorek, Zh. Zhou, D. Qian, R. Mannava and V.K. Vasudevan // *Mater. Sci. Eng. A* **613** (2014) 274.
- [66] W. Wang, S. Lartigue-Korinek, F. Brisset, A.L. Helbert, J. Bourgon and T. Baudin // *J. Mater. Sci.* **60** (2015) 2167.
- [67] I. Borgh, P. Hedström, A. Blomqvist, J. Lgren and J. Odqvist // *Acta Mater.* **66** (2014) 209.
- [68] S.G. Vadchenko, A.E. Sytshev, D. Yu. Kovalev, A.S. Shchukin and S.V. Konovalikhin // *Nanotechnologies in Russia* **10** (2015) 67.